Draft version October 16, 2017
Typeset using LaTeX **twocolumn** style in AASTeX61

GALAXIES PROBING GALAXIES IN PRIMUS – I. SAMPLE, SPECTROSCOPY, AND CHARACTERISTICS OF THE $z \sim 0.5$ MG II-ABSORBING CIRCUMGALACTIC MEDIUM

Kate H. R. Rubin,[1] Aleksandar M. Diamond-Stanic,[2] Alison L. Coil,[3] Neil H. M. Crighton,[4] and John Moustakas[5]

[1] *San Diego State University, Department of Astronomy, San Diego, CA 92182, USA*
[2] *Bates College, Department of Physics & Astronomy, 44 Campus Ave, Carnegie Science Hall, Lewiston, ME 04240, USA*
[3] *Center for Astrophysics and Space Sciences, Department of Physics, University of California, San Diego, 9500 Gilman Drive, La Jolla, CA 92093, USA*
[4] *Australian Competition and Consumer Commission, Melbourne, VIC 3001; Center for Astrophysics and Supercomputing, Swinburne University of Technology, Hawthorn, VIC 3122, Australia*
[5] *Department of Physics and Astronomy, Siena College, 515 Loudon Road, Loudonville, NY 12211, USA*

(Accepted to ApJ September 22, 2017)

ABSTRACT

Spectroscopy of background QSO sightlines passing close to foreground galaxies is a potent technique for studying the circumgalactic medium (CGM). QSOs are effectively point sources, however, limiting their potential to constrain the size of circumgalactic gaseous structures. Here we present the first large Keck/LRIS and VLT/FORS2 spectroscopic survey of bright ($B_{\rm AB} < 22.3$) background galaxies whose lines of sight probe Mg II $\lambda\lambda 2796, 2803$ absorption from the CGM around close projected foreground galaxies at transverse distances 10 kpc $< R_\perp <$ 150 kpc. Our sample of 72 projected pairs, drawn from the PRIsm MUlti-object Survey (PRIMUS), includes 48 background galaxies which do not host bright AGN, and both star-forming and quiescent foreground galaxies with stellar masses $9.0 < \log M_*/M_\odot < 11.2$ at redshifts $0.35 < z_{\rm f/g} < 0.8$. We detect Mg II absorption associated with these foreground galaxies with equivalent widths 0.25 Å $< W_{2796} <$ 2.6 Å at $> 2\sigma$ significance in 20 individual background sightlines passing within $R_\perp < 50$ kpc, and place 2σ upper limits on W_{2796} of $\lesssim 0.5$ Å in an additional 11 close sightlines. Within $R_\perp < 50$ kpc, W_{2796} is anticorrelated with $R_\perp$, consistent with analyses of Mg II absorption detected along background QSO sightlines. Subsamples of these foreground hosts divided at $\log M_*/M_\odot = 9.9$ exhibit statistically inconsistent W_{2796} distributions at 30 kpc $< R_\perp <$ 50 kpc, with the higher-M_* galaxies yielding a larger median W_{2796} by 0.9 Å. Finally, we demonstrate that foreground galaxies with similar stellar masses exhibit the same median W_{2796} at a given $R_\perp$ to within < 0.2 Å toward both background galaxies and toward QSO sightlines drawn from the literature. Analysis of these datasets constraining the spatial coherence scale of circumgalactic Mg II absorption is presented in a companion paper.

Keywords: galaxies: halos — galaxies: absorption lines — quasars: absorption lines

Corresponding author: Kate H. R. Rubin
krubin@sdsu.edu

1. INTRODUCTION

QSO absorption line spectroscopy has for nearly half a century been our principal and most powerful tool for the study of diffuse baryons. From measurement of the incidence and metallicity of material in the most rarefied intergalactic regions (Simcoe et al. 2004; Lehner et al. 2007; Danforth & Shull 2008) to detailed constraints on the kinematics, ionization state, metal content, and mass of highly metal-enriched superwind ejecta close to massive galaxies (e.g., Tripp et al. 2011), spectroscopy of bright QSOs has revealed the nature of "dark" gaseous material in virtually all galactic and intergalactic environments. Experiments which search the sky for QSO sightlines close in projection to foreground galaxies have been designed to assess the properties of gas in the circumgalactic medium (CGM) surrounding a wide variety of galaxy hosts, from sub-luminous dwarfs (Prochaska et al. 2011; Burchett et al. 2015; Bordoloi et al. 2014; Rubin et al. 2015) to luminous red galaxies and massive QSO hosts (Prochaska et al. 2013a; Farina et al. 2014; Zhu et al. 2014; Johnson et al. 2015). The assembly of large samples of such background QSO - foreground galaxy pairs provides a statistical picture of the absorption exhibited by the targeted foreground galaxy environment (e.g., Churchill et al. 2000; Chen et al. 2001; Adelberger et al. 2005; Chen et al. 2010a; Werk et al. 2013).

At $z \lesssim 2$, the vast majority of QSO-galaxy pair studies have focused primarily (and in many cases, exclusively) on measurement of the absorption strength of the Mg II $\lambda\lambda 2796, 2803$ doublet. This transition, accessible from the ground at $z \gtrsim 0.2$, arises from cool, photoionized gas at a temperature $T \sim 10^4$ K (Bergeron & Stasińska 1986), and is sensitive enough to yield large equivalent widths ($W_{2796} > 0.1$ Å) in sightlines having neutral hydrogen column densities as low as $N(\mathrm{H\ I}) \gtrsim 10^{16.5}\mathrm{cm}^2$ (e.g., Lehner et al. 2013). Such studies have demonstrated that $\sim L^*$ galaxies at $z \lesssim 0.5$ are enveloped by Mg II-absorbing gas extending to radii $R_{\mathrm{MgII}} \sim 100$ kpc (Chen et al. 2010a). Within this region, Mg II absorbers having $W_{2796} > 0.1$ Å arise with an incidence $C_f \sim 80\%$. Recent work has suggested a higher incidence of stronger absorption around galaxies with higher stellar masses (Chen et al. 2010a; Churchill et al. 2013). Finally, experiments leveraging quantitative morphological measurements of the targeted foreground systems suggest the strongest Mg II absorbers occur toward QSOs located close to (i.e., within $\Phi \lesssim 45°$ of) the minor axis of the host galaxy (Bouché et al. 2012; Kacprzak et al. 2012; Nielsen et al. 2015).

While such studies have proven very fruitful, they have nevertheless relied exclusively on a single tool: the $10^{-3}-10^{-2}$ pc beam of UV-bright continuum emitted by the accretion disks powering luminous QSOs (Shakura & Sunyaev 1973; Frank et al. 2007). Due to the extremely small scale of this beam, QSO spectroscopy cannot directly distinguish between compact clouds with volumes less than a cubic parsec and elongated filaments stretching over many kiloparsecs – and hence cannot be used to bring such geometrical constraints to bear on the physical origin of this material.

There is ample evidence demonstrating that cool gas traced by Mg II absorption is launched away from star-forming regions in galactic winds (Weiner et al. 2009; Rubin et al. 2010b; Martin et al. 2012; Rubin et al. 2014); however, the relation between this material and the Mg II-absorbing structures detected at $R_\perp > 10$ kpc has not been established. Moreover, there is a strong theoretical expectation of the presence of an additional, hotter gas phase ($T \sim 10^6$ K) filling the same extended halos, fed by the virial shock front formed by accreting material (Rees & Ostriker 1977; Kereš et al. 2005). If this hot phase is indeed ubiquitous, a cool cloud passing through it will be destroyed on a timescale which is approximately linearly dependent on its size (Schaye et al. 2007; Crighton et al. 2014; McCourt et al. 2015). Constraints on the scale of this material therefore in principle also constrain the structure lifetime as a function of its relative velocity. Such estimates may be used to test the viability of several presumptive origins for the cool CGM, including the cool winds described above (e.g., Bond et al. 2001; Steidel et al. 2010; Bouché et al. 2012), infalling cold streams (e.g. Kereš et al. 2005; Kacprzak et al. 2012; Bouché et al. 2013; Crighton et al. 2013), or condensation of the hot halo material via thermal instability (Maller & Bullock 2004; Binney et al. 2009).

Absorption spectroscopy toward background probes having a wide range in the projected spatial extent of their UV continuum emission can, however, reveal the small-scale structure of the cool CGM. Galaxies, with typical sizes $>$ kpc[2], are now being used as bright background sources in a growing number of studies (Adelberger et al. 2005; Barger et al. 2008; Rubin et al. 2010a; Steidel et al. 2010; Lee et al. 2014; Bordoloi et al. 2011; Diamond-Stanic et al. 2015; Cooke & O'Meara 2015; Lee et al. 2016). In principle, spatially-resolved spectroscopy of such extended background beams probe variations in absorption strength and kinematics along multiple independent sightlines. As we will demonstrate in the second paper of this series (Rubin et al. 2017, in prep; hereafter cited as Paper II), even if it is not possible to resolve the beam, an analysis comparing the properties of absorbers observed along integrated spectra of background

galaxies and QSOs provides a direct constraint on the coherence scale of the cool absorption.

To facilitate these experiments, large spectroscopic galaxy redshift surveys may be searched for projected pairs of systems in analogy to targeted QSO-galaxy pair searches. While the spectral signal-to-noise achieved in the vast majority of redshift surveys is insufficient to assess foreground absorber properties along individual background galaxy sightlines, many of the studies listed above have coadded background galaxy spectra in the rest-frame of the foreground system in each pair for constraints on the mean foreground absorption equivalent width (e.g., Steidel et al. 2010; Bordoloi et al. 2011). Only a handful of studies have achieved the S/N required to securely detect foreground absorption in individual sightlines, and each of these works report on just one or two projected pairs (Adelberger et al. 2005; Barger et al. 2008; Rubin et al. 2010a; Diamond-Stanic et al. 2015; Cooke & O'Meara 2015). Indeed, the sizes of these samples have been severely limited by the scarcity of galaxies which are both sufficiently bright to obtain S/N $\gtrsim 5$ Å^{-1} spectroscopy in the near-UV, and which are located within $\lesssim 100$ projected kpc of a foreground galaxy whose redshift is known *a priori*. In principle, however, a redshift survey covering a large sky volume at high density can yield significant numbers of such pairs. The background sightlines may then be reobserved with UV-sensitive instrumentation to achieve high-S/N constraints on foreground absorbers, the vast majority of which arise due to H I and metal-line transitions at rest wavelengths blueward of 3000 Å.

Such a high-volume, high-density redshift survey is now available in PRIMUS, the PRIsm MUlti-object Survey (Coil et al. 2011b). Here we present high-S/N Keck/LRIS and VLT/FORS2 rest-frame near-UV spectroscopy of 72 projected pairs of galaxies having impact parameters $R_\perp < 150$ kpc identified in the PRIMUS redshift catalog. Our galaxy pair sample, spanning the redshift range $0.4 \lesssim z \lesssim 1.0$, includes 49 pairs with projected separations $R_\perp < 50$ kpc, thoroughly sampling the "inner" CGM which typically gives rise to strong Mg II absorbers having $W_{2796} > 0.3$ Å (e.g., Chen et al. 2010a). The foreground galaxies in our sample span the star-forming sequence to a stellar mass limit $\gtrsim 10^9\ M_\odot$, and at high stellar masses ($M_* \gtrsim 10^{10.5}\ M_\odot$) include both star-forming and quiescent systems. These data permit the first investigation of the absorption strength of the Mg II λ2796 transition to a limiting $W_{2796} \gtrsim 0.5$ Å associated with foreground galaxy halos in a statistical sample of individual background galaxy sightlines. We explore the dependence of this W_{2796} on intrinsic galaxy properties (i.e., star formation rate, M_*) as a function of $R_\perp$, and compare these measurements to those drawn from QSO-galaxy pair studies in the literature. In a companion paper (Paper II), we take advantage of all of these data to develop direct constraints on the spatial extent of the cool material giving rise to the observed Mg II absorption, and use this analysis to address the lifetime and fate of these structures.

We describe our sample selection in Section 2, and describe our observations and data reduction procedures in Section 3. Section 4 details our methods of redshift estimation and absorption line analysis. We present salient properties of our foreground and background galaxy samples in Sections 5 and 6. Section 7 describes our results on the relationship between the Mg II absorption strength in the CGM and the intrinsic host galaxy properties, and compares these findings to the results of previous QSO-galaxy and galaxy-galaxy pair studies. We present a brief summary in Section 8. Throughout, we adopt a ΛCDM cosmology with $H_0 = 70$ km s^{-1} Mpc^{-1}, $\Omega_{\rm M} = 0.3$, and $\Omega_\Lambda = 0.7$. Magnitudes are quoted in the AB system.

2. SAMPLE SELECTION

2.1. *PRIMUS Galaxy Pairs*

Our galaxy pair sample is drawn from PRIMUS, a spectroscopic survey of galaxies with redshifts in the range $0 < z < 1.2$ (Coil et al. 2011b; Cool et al. 2013). Using the IMACS instrument on the Magellan Baade Telescope (Bigelow & Dressler 2003), PRIMUS obtained redshifts for $\sim 120,000$ galaxies over 9.1 deg^2 to a magnitude limit $i \sim 23$. The PRIMUS sample is distributed over seven "science" fields selected to have existing ancillary multi-wavelength imaging: the Chandra Deep Field South-SWIRE field (CDFS-SWIRE; Giacconi et al. 2001), the DEEP2 fields at 23hr and 02hr (Davis et al. 2003), the COSMOS field (Ilbert et al. 2009), the *XMM*-Large Scale Structure Survey field (XMM-LSS; Pierre et al. 2004), the European Large Area ISO Survey-South 1 field (Oliver et al. 2000), and the Deep Lens Survey F5 field (Wittman et al. 2002).

We used four main criteria to select our primary sample of projected galaxy pairs from this parent catalog for follow-up spectroscopy in the near-UV:

1. First, we considered all galaxies having a PRIMUS redshift $z^{\rm PR} \geq 0.35$ with high confidence (i.e., a redshift confidence flag $Q = 3$ or 4) to ensure spectral coverage of Mg II $\lambda\lambda$2796, 2803 absorption within the wavelength range at which LRIS and FORS2 have optimum sensitivity ($\lambda \gtrsim 3700$ Å). The low-dispersion prism used to carry out the PRIMUS survey yields a redshift accuracy of

$\sigma_z/(1+z) = 0.0051$ for objects assigned these confidence flags, with an outlier rate of objects having $\Delta_z/(1+z) > 0.03$ of 8% (Coil et al. 2011b).

2. We then selected pairs of these objects with projected separations $R_\perp \leq 50$ kpc at the $z^{\rm PR}$ value of the foreground (f/g) galaxy, and further required that the redshift offset between the f/g and background (b/g) galaxies satisfies $z^{\rm PR}_{\rm b/g} - z^{\rm PR}_{\rm f/g} \geq 0.02$ (corresponding to a velocity difference $\gtrsim 3500$ km s^{-1}).

3. We required that the b/g galaxy have an apparent B-band magnitude sufficient to yield a 3σ W_{2796} detection limit of 0.5 Å at $z^{\rm PR}_{\rm f/g}$ in an exposure time < 2.5 hours with LRIS or FORS2. All b/g galaxies satisfying this criterion have $B_{\rm AB} < 22.3$.

4. We finally demanded that each f/g galaxy have an apparent B-band magnitude sufficient to yield a 3σ W_{2796} detection limit of 1.5 Å toward its own stellar continuum within 2.5 hours of exposure time. This corresponds to an approximate magnitude limit of $B_{\rm AB} \lesssim 23.3$, and permits both higher-resolution spectroscopic confirmation of $z^{\rm PR}_{\rm f/g}$ as well as detailed analysis of "down-the-barrel" absorption for comparison with halo gas kinematics observed toward the b/g galaxy.

In the five PRIMUS science fields that we targeted in this study (the two DEEP2 fields, the XMM-LSS field, the COSMOS field, and the CDFS-SWIRE field), there are 78 pairs of galaxies that satisfy these criteria. We selected 58 pairs from among this sample to observe in the rest-frame near-UV, prioritizing brighter pairs, those having $\delta z^{\rm PR} = z^{\rm PR}_{\rm b/g} - z^{\rm PR}_{\rm f/g} \geq 0.1$, and pairs which are close on the sky such that they could be observed simultaneously in multislit mode. These objects are listed in Table 1, along with their redshifts, apparent magnitudes, and angular separations, and are indicated with three-digit identification numbers. Due to the occasional underestimation of the uncertainty in the redshifts determined from the low-dispersion PRIMUS discovery spectra, five of these pairs having $\delta z^{\rm PR} \approx 0.03 - 0.13$ were identified as physical (i.e., not projected) in our followup observations, with $|z_{\rm b/g} - z_{\rm f/g}| < 0.003$ (where $z_{\rm b/g}$ and $z_{\rm f/g}$ are galaxy redshifts estimated from our LRIS and FORS2 spectroscopy as described in §4.1). Two additional pairs were found to include stellar (Galactic) sources.

We also obtained spectra of 32 serendipitous pairs, most of which have larger (50 kpc $< R_\perp <$ 150 kpc) projected separations. These pairs were targeted for their exceptionally bright b/g objects, or where they could be included on the same slitmask with a primary (close) pair target. These objects are indicated in Table 1 with identification numbers greater than 1000.

2.2. *QSO-Galaxy Comparison Pairs*

In the analysis to follow, we also draw on published samples of galaxies for which the circumgalactic Mg II absorption has been well-characterized using background QSO sightlines. We select these QSO-galaxy pair measurements based on the experimental design of the work in which they are reported. That is, we require these samples to be designed using a methodology as similar as possible to that of our PRIMUS pairs experiment. Because our PRIMUS b/g sightlines are selected without prior knowledge of f/g Mg II absorption, the selected QSO-galaxy samples must also be designed without such prior knowledge. Including absorption-selected systems would tend to yield higher overall W_{2796} profiles, and so would introduce a bias into our comparison of these datasets. We choose to include measurements from the two largest available QSO-galaxy pair studies with the appropriate experimental design: the 69 pairs probing "isolated" galaxies studied in Chen et al. (2010a), and the 39 pairs composing the COS-Halos sample (Werk et al. 2013). Both of these works focus on the gaseous environments of $\sim L^*$ galaxies at low redshift, and hence offer a comparison sample with quite similar f/g galaxy properties to those selected from PRIMUS (see §5 for further detail).

3. SPECTROSCOPIC OBSERVATIONS AND SUPPLEMENTARY DATA

Our follow-up spectroscopy was carried out with two instruments: the Low Resolution Imaging Spectrometer (LRIS) on Keck 1 (Cohen et al. 1994), and the FOcal Reducer/low dispersion Spectrograph 2 (FORS2) on VLT-UT1 (Appenzeller et al. 1998). Primary pair targets requiring exposure times longer than 1 hr were observed in multislit mode in most cases. We chose longslit mode for the remaining targets.

3.1. *Keck/LRIS Spectroscopy*

Keck/LRIS observations were carried out during three observing runs on 2011 Oct 1 UT, 2012 Jan 20-21 UT, and 2012 Dec 13-15 UT. Seeing conditions on these dates varied over the range FWHM $\sim 0.5 - 1.5''$. A slit width of $1''$ was used for both **multislit** and longslit observations. We used the 600 l mm^{-1} grism blazed at 4000 Å on the blue side and the 600 l mm^{-1} grating blazed at 7500 Å on the red side with the D560 dichroic, obtaining full wavelength coverage between $\sim$ 3200 Å and $\sim$ 8450 Å. The velocity resolution of the spectra is

FWHM ~ 160 km s^{-1} at 8000 Å, degrading to FWHM ~ 345 km s^{-1} at 3500 Å.

All fields observed in multislit mode are listed in Table 2, along with the ID of the pairs on each slitmask and the date of observation. Total exposure times ranged between 0.4 and 3.2 hrs. Individual exposures were typically $\sim 1200 - 1800$ sec in length on the blue side and $\sim 400 - 900$ sec in length on the red. Pairs observed in longslit mode are listed in Table 3, with integration times ranging from 0.4 to 1.8 hrs.

3.2. *VLT/FORS2 Spectroscopy*

Our VLT/FORS2 program (with ESO program IDs 088.A-0529A and 090.A-0485A) was carried out in visitor mode over three nights on 2011 Nov 25 UT and 2012 Nov 14-15 UT. Seeing conditions were excellent for two of these nights (FWHM $\sim 0.5 - 0.7''$) and varied between 1 and $2''$ on 2012 Nov 14. A slit width of $1''$ was chosen in both longslit and multislit (MXU) mode. We observed with the blue-sensitive E2V CCDs, using the GRIS_1200B grism to obtain coverage between 3670 and 5120 Å. We additionally observed each mask and longslit pointing with one of two red-sensitive grisms: GRIS_600V or GRIS_600RI. These latter setups cover from 4530 to 7510 Å and from 5150 to 8470 Å, respectively, providing spectroscopy of nebular emission lines and Balmer absorption at rest-frame wavelengths $3700 - 5010$ Å. The GRIS_1200B grism yields a velocity resolution FWHM ~ 155 km s^{-1} near 5000 Å and ~ 185 km s^{-1} at 3670 Å, while both of the red grisms provide a median resolution FWHM ~ 250 km s^{-1}.

The fields observed in MXU mode are listed toward the bottom of Table 2. Exposure times for spectra taken with the GRIS_1200B grism are listed in the 5th column, and range between 0.7 and 3 hrs. The length of exposures taken with the red grisms in place are listed in the 6th column, and are all between 15 and 30 min. The three pairs observed with the FORS2 longslit are included in Table 3, and were observed for 0.4-0.9 hrs and 15-30 min with the GRIS_1200B and GRIS_600V setups, respectively.

Both LRIS and FORS2 data were reduced using the XIDL LowRedux[1] data reduction pipeline. The pipeline includes bias subtraction, flat-fielding, slit finding, wavelength calibration, object identification, sky subtraction, and relative flux calibration. Wavelength calibrations were adjusted for flexure by applying an offset estimated from the cross-correlation of the sky spectrum with a sky spectral template. Wavelengths for the final, coadded one-dimensional spectra are in vacuum and have been corrected to the heliocentric frame.

3.3. *Supplementary Data*

As detailed in Coil et al. (2011b), the PRIMUS survey fields have been deeply imaged in multiple broad passbands. The XMM-LSS, CDFS-SWIRE, DEEP2 02h, DEEP2 23h, and COSMOS fields have all been observed in the near- and far-UV by *GALEX*, and with the exception of the DEEP2 23h field have also been imaged in four *Spitzer*/IRAC passbands. Each of these fields has been imaged over the full optical range from ground-based facilities.

Together with PRIMUS survey redshifts, Moustakas et al. (2013) have assembled these photometric measurements to produce broadband spectral energy distributions (SEDs) for the full PRIMUS galaxy sample. These authors have also developed a custom suite of routines (`iSEDfit`[2]) to model these SEDs via stellar population synthesis, calculating rest-frame magnitudes and colors and constraining star formation histories. In brief, `iSEDfit` adopts the Flexible Stellar Population Synthesis models of Conroy & Gunn (2010) with a Chabrier (2003) IMF. Star formation histories are assumed to be exponentially declining with added stochastic bursts. The resulting library of model SEDs covers a broad range of ages, metallicities, burst timing and strength, and dust attenuation. This parameter space is then sampled to calculate the marginalized probability distribution functions for stellar mass (M_*) and star formation rate (SFR). In the present work, we use the same photometric catalogs and procedures described above (and in full in Moustakas et al. 2013) to constrain these quantities, adopting the galaxy redshifts estimated from our LRIS and FORS2 spectroscopy as described in §4.1. The typical uncertainties on the values of $\log M_*/M_\odot$ and log SFR estimated for the parent PRIMUS sample using this method are 0.08 dex and 0.2 dex, respectively (Mendez et al. 2016).

The COSMOS field, in which 30 of the observed pairs in our sample are located, has also been imaged by the *HST* Advanced Camera for Surveys (ACS) in the F814W filter to a 5σ depth of $I_{\rm AB} = 28$ mag for point sources (Scoville et al. 2007). We use the publicly available mosaic imaging provided by the COSMOS team with a pixel scale $0.03''$pix^{-1}. Small ($25'' \times 25''$) sections of this imaging showing each of the pairs for which our spectroscopy of the b/g object covers Mg II at the foreground redshift $z_{\rm f/g}$ (and for which $c(z_{\rm b/g} - z_{\rm f/g})/(1 + z_{\rm pair}) >$

[1] http://www.ucolick.org/~xavier/LowRedux/

[2] **http://www.sos.siena.edu/~jmoustakas/isedfit/**

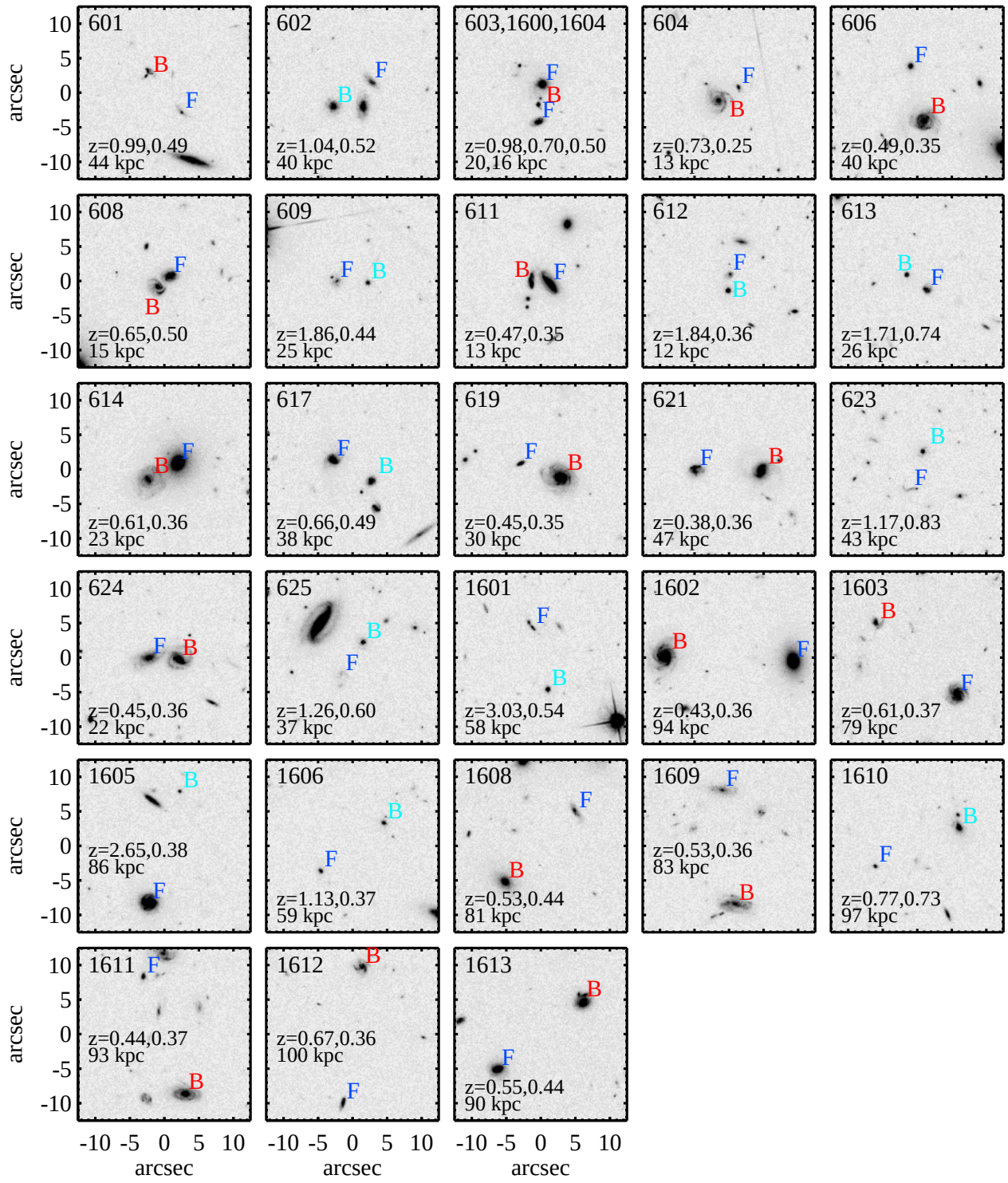

Figure 1. *HST*/ACS F814W-band imaging of projected pairs of galaxies for which we have obtained deep near-UV spectroscopy in the COSMOS field (Scoville et al. 2007). Each panel is 25″ × 25″. Background objects are indicated with a cyan "B" if they exhibit broad-line AGN emission and are marked with a red "B" in the remaining cases. All foreground objects are indicated with a blue "F". The images are labeled with the corresponding pair IDs at upper left, with the galaxy redshifts and projected separation of each pair listed at lower left.

1000 km s^{-1}, with $z_{\rm pair} = (z_{\rm b/g} + z_{\rm f/g})/2)$, are shown in Figure 1.

4. SPECTROSCOPIC ANALYSIS

4.1. *Redshifts*

The following analysis associates Mg II-absorbing material observed along a background galaxy or QSO sightline with a nearby "host" galaxy. We draw this association based on the relative kinematics of the galaxies and absorbers, and thus require precise measurements of the foreground galaxy redshifts (with uncertainties $c\sigma_z/(1+z) < 100$ km s^{-1}). As the accuracy of PRIMUS redshifts is $c\sigma_z/(1+z) \approx 1500$ km s^{-1}, and because there is a non-negligible outlier rate for the sample of interest (in particular because galaxies which are close on the sky are more likely to be physically associated than a pair of galaxies selected at random), we analyze our follow-up spectroscopy to improve the precision of both our f/g and b/g galaxy redshift estimates.

We use IDL routines adapted from the DEEP2 data reduction pipeline[3] to perform these redshift measurements. For this analysis, we enable the pipeline to accept a redshift estimated by eye as an initial guess. The code then determines the best-fit offset between the observed spectrum and a linear combination of a nebular emission-line template, an early-type galaxy spectrum, a post-starburst galaxy spectrum, and the spectrum of a broad-line AGN (as in Coil et al. 2011a). This best-fit offset is determined from the blue and red spectrum of each object independently. The portion of each spectrum blueward of $\lambda_{\rm rest} < 3000$ Å was masked prior to fitting for all foreground galaxies to prevent intrinsic kinematic offsets (due to, e.g., winds or inflows) from biasing the measurements. Redshifts estimated from the red spectra are adopted in most cases, with blue spectra providing redshifts for a few objects with low S/N red coverage. The dispersion in redshifts measured from the red vs. blue spectra for our foreground galaxy sample (i.e., the dispersion in the quantity $c(z_{blue} - z_{red})/(1+z_{red})$) is 86 km s^{-1}. We consider this a conservative upper bound on our redshift measurement uncertainty, as these offsets are systematically affected by the large difference in spectral coverage as well as occasional significant differences in S/N in the spectra taken from the two cameras/grisms of LRIS and FORS2.

4.2. *Spectroscopic Data Quality*

Among the 59 primary sample pairs observed, there are 3 pairs for which the S/N of the foreground galaxy spectrum is insufficient to yield a high-quality redshift measurement (pairs 216, 419, and 605). There are seven more primary sample pairs for which at least one of the PRIMUS redshift estimates was in error, and yielded physically-associated systems or stellar sources. This leaves a sample of 49 *bona fide* projected galaxy pairs having $R_\perp < 50$ kpc in our primary sample with high-quality spectroscopic redshifts. There are an additional 25 serendipitous pairs, 23 at larger impact parameters (50 kpc $< R_\perp <$ 150 kpc), and 2 of which have $R_\perp < 50$ kpc (pairs 1600 and 1604), which our spectra confirm to be extragalactic objects in projection.

The spectroscopy of the b/g galaxies in two of the $R_\perp > 50$ kpc pairs does not extend blueward of 2800 Å at the systemic velocity of the corresponding f/g object measured as described above, and so must be expunged from the sample. Hence, our dataset includes a total of 72 projected pairs (51 of them having $R_\perp < 50$ kpc) with spectroscopic coverage of the Mg II doublet at $z_{\rm f/g}$. Figure 2 shows representative spectroscopy of three of the sample b/g galaxies in close pairs, with strong Mg II and Fe II transitions at the systemic velocities of the b/g and f/g galaxies marked in red and blue, respectively.

The median S/N measured in a velocity window $\delta v \pm 500$ km s^{-1} around the observed wavelength of the Mg II λ2796 transition at $z_{\rm f/g}$ ($\lambda_{2796}^{\rm f/g}$) in our b/g galaxy spectra is shown in Figure 3 versus the apparent B-band magnitude of the b/g object (left). Close pairs are indicated with large orange squares, and pairs having $R_\perp > 50$ kpc are marked with small blue squares. Those b/g galaxies for which the best-fitting redshift template spectrum was that of the broad-line AGN (and those exhibiting any broad-line Mg II emission obvious in a visual inspection) are outlined in magenta. The S/N of this spectroscopy ranges from $\sim 2-40$ Å^{-1}, and tends to increase with the brightness of the b/g object. The spectra of the objects hosting broad-line AGN have overall higher S/N, with a median S/N = 16.1 Å^{-1} (vs. a median S/N = 9.0 Å^{-1} for the remaining b/g galaxies).

We compare this S/N with $z_{\rm f/g}$ in the right-hand panel of Figure 3. The redshift distribution of the f/g galaxy sample peaks toward the lower limit of our selection criterion for $z^{\rm PR}$, with the median $z_{\rm f/g} = 0.44$ for both the close pair sample and the full sample of pairs. Moreover, the S/N in the background sightlines is uncorrelated with $z_{\rm f/g}$, indicating that the drop in efficiency of the spectrographs blueward of 4000 Å is not significantly affecting our sensitivity to foreground absorption for the lower-$z_{\rm f/g}$ portion of the sample.

4.3. *Absorption Equivalent Widths and Velocity Centroids*

[3] http://deep.ps.uci.edu/spec2d

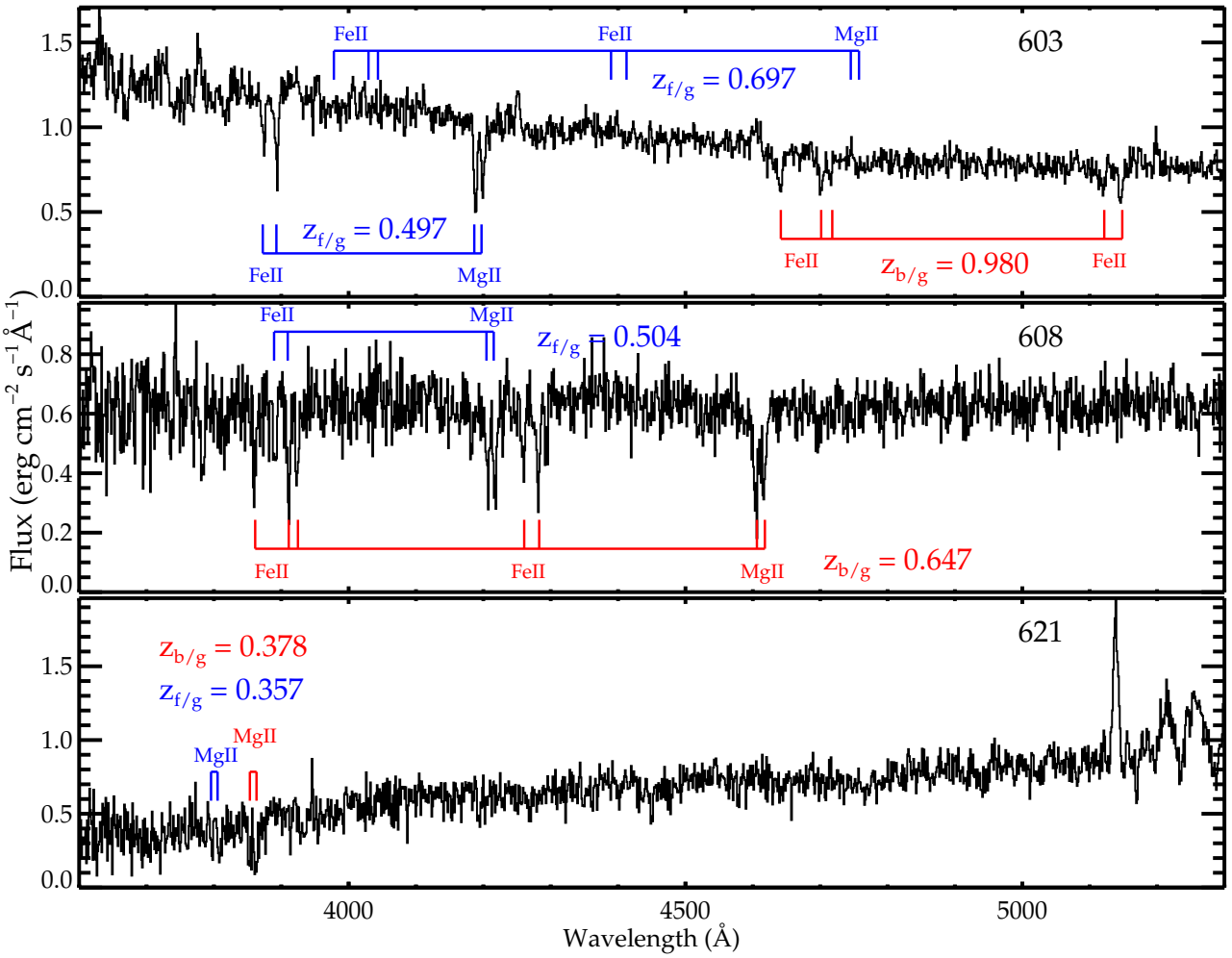

Figure 2. Spectroscopy of the b/g galaxy in three of the close ($R_\perp < 50$ kpc) pairs in our sample, with pair ID numbers indicated at upper right. Subsets of the transitions Mg II $\lambda\lambda 2796, 2803$, Fe II $\lambda\lambda 2586, 2600$, and Fe II $\lambda\lambda 2344, 2374, 2382$ at the systemic velocity of the b/g galaxy are marked in red. Wherever spectroscopic coverage is available, the same transitions are marked in the rest-frame of the corresponding f/g galaxy in blue. The spectrum shown in the top panel probes f/g systems within 50 kpc at two redshifts ($z_{\rm f/g} = 0.697$ and $z_{\rm f/g} = 0.497$ in pairs 603 and 1600, respectively). The spectra span the range in S/N at $\lambda_{2796}^{\rm f/g}$ of the b/g galaxy spectroscopy in our sample, with S/N(Mg II) = 19.1 Å^{-1} (top), 15.8 Å^{-1} (middle), and 6.4 Å^{-1} (bottom).

Prior to making measurements of the absorption strength in rest-frame UV transitions arising in the CGM of the f/g galaxy sample, we normalize each background galaxy spectrum to the level of the continuum. The majority of our b/g objects are dominated by stellar continuum emission blueward of $\lambda_{\rm rest}^{\rm b/g} \sim 3700$ Å, such that their spectra are relatively flat and featureless in the wavelength range of interest. In these cases, the continuum level is determined via a linear fit to the data in the spectral regions on either side of each feature. In particular, a fit to the data in the windows $(2765-2785)\times(1+z_{\rm f/g})$Å and $(2810-2830)\times(1+z_{\rm f/g})$ Å is assumed to describe the continuum level at $\lambda_{2796}^{\rm f/g}$. We visually inspected these regions in each b/g galaxy spectrum to ensure they do not include strong emission or absorption features associated with the b/g object, and made small adjustments to their boundaries to avoid such features in several cases. For each spectrum, we also generate 1000 Monte Carlo realizations of this continuum fit by first adding Gaussian random noise with a dispersion given by the median error in the data to the original fit, and then fitting a line to each of these continuum realizations. This allows us to assess the degree of uncertainty in the continuum level. We

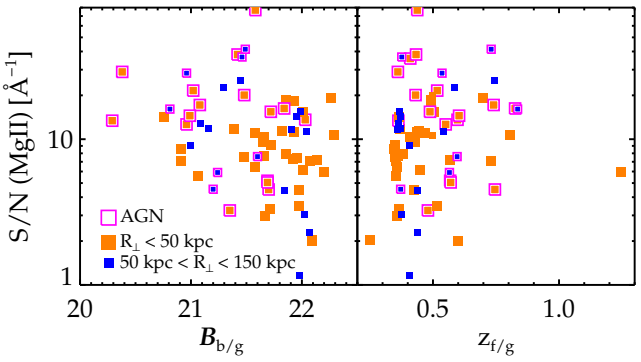

Figure 3. *Left:* S/N measured in each b/g galaxy spectrum within $\delta v < 500$ km s^{-1} of the Mg II 2796 transition in the rest frame of the close projected f/g galaxy ($\lambda_{2796}^{f/g}$) vs. the apparent B-band magnitude of the b/g object. Large orange squares indicate pairs with impact parameters < 50 kpc, and small blue squares mark pairs with larger separations. Symbols outlined in magenta correspond to b/g sightlines dominated by emission from a broad-line AGN. *Right:* S/N measured at $\lambda_{2796}^{f/g}$ vs. $z_{f/g}$. Symbol shapes and colors are consistent with those in the left-hand panel. The S/N of our spectroscopy ranges from $\sim 2-40$ Å^{-1}, with the median S/N for those b/g objects without dominant broad-line AGN ≈ 9.0 Å^{-1}.

find that the dispersion in the W_{2796} values (calculated as described below) measured after adopting this set of continuum fits is typically only $\sim 40\%$ of the formal uncertainty in W_{2796} given by the square root of the sum of variances in each absorption-line pixel.

Twelve of the b/g objects in our sample are host to bright QSOs, and their continua are dominated by the complex broad emission line features typical of such systems. In these cases, the continuum level was determined using a custom routine available in the XIDL software package[4]. The routine (x_continuum) facilitates a by-eye spline fit to the full QSO spectrum. Previous studies invoking this technique have found the average uncertainty in the resulting continua is $\lesssim 5\%$ outside of the Lyα forest (Prochaska et al. 2013b).

After continuum normalization, we search the spectral region within $\delta v \pm 300$ km s^{-1} of $\lambda_{2796}^{f/g}$ and $\lambda_{2803}^{f/g}$ by eye to identify absorption associated with each transition. We select the velocity range spanning the absorption profiles by hand, and then perform a boxcar sum over this range to calculate W_{2796} and W_{2803}. We also flag any profiles which are affected by blending with absorption transitions associated with the b/g galaxy itself, or which (in the case of two of our serendipitous pairs) are blended with the Lyα forest. We additionally calculate the flux-weighted wavelength centroid of each Mg II 2796 profile, $\langle\lambda_{2796}\rangle = \sum_i(1-f_i)\lambda_i / \sum_i(1-f_i)$, with f_i and λ_i the normalized flux and wavelength of each pixel within the line. Our measurements of W_{2796}, W_{2803}, and the velocity offset between $\langle\lambda_{2796}\rangle$ and $z_{f/g}$ ($\langle\delta v_{2796}\rangle$) are listed in Table 4. Our spectroscopic coverage of Mg II at $z_{f/g}$ along each background galaxy sightline is shown in Appendix A for reference. We detect unblended Mg II λ2796 absorption securely (at $> 2\sigma$ significance) in 20 individual background sightlines having $R_\perp < 50$ kpc, with W_{2796} values in the range 0.25 Å $< W_{2796} <$ 2.6 Å. We place 2σ upper limits on W_{2796} of $\lesssim 0.5$ Å in an additional 11 close sightlines.

[4] www.ucolick.org/~xavier/IDL

5. FOREGROUND GALAXY PHYSICAL PARAMETERS

Having estimated rest-frame colors, luminosities, SFRs and stellar masses for our foreground galaxy sample as described in Section 3.3, we now examine these properties in the context of the $z \sim 0.5$ galaxy population. Figure 4 (left) shows the distribution of rest-frame $U-B$ color and absolute B-band magnitude of these objects with colored points. Symbols outlined in magenta mark pairs in which the b/g galaxy hosts a bright AGN. These latter pairs should be considered QSO-galaxy pairs, albeit with fainter b/g sightlines than are typically used, whereas the former are *bona fide* galaxy-galaxy pairs in which the b/g sightline is not dominated by a bright nuclear source. Six pairs for which our coverage of Mg II λ2796 at $z_{f/g}$ is affected by line blending are excluded here (and from all following analysis; these objects are indicated in the column reporting W_{2796} in Table 4). The black contours and gray shading indicate the distribution of all galaxies with high-quality redshift measurements in the PRIMUS catalog at $0.35 < z^{PR} < 0.8$, with the degree of shading scaled to the density of objects. The SFR-stellar mass distributions for the same galaxy samples are shown at right. A small minority of the f/g objects in our close pair sample lie along the "red sequence" in the color-magnitude diagram (e.g., Willmer et al. 2006) and exhibit low SFRs ($\lesssim 0.1-1\ M_\odot$ yr^{-1}), while the majority of the sample lies along the main locus of the star-forming sequence at $z \sim 0.4-0.8$. In the following analysis, we adopt the fit to the minimum of the bimodal galaxy distribution in the parent PRIMUS survey reported by Berti et al. (2016) as the dividing line between the star-forming and quiescent objects:

$$\log \mathrm{SFR} = -1.29 + 0.65(\log \frac{M_*}{M_\odot} - 10) + 1.33(z-0.1), \quad (1)$$

with SFR having units of $M_\odot$ yr^{-1}. Thus, the SFR dividing the star-forming sequence from the locus of quiescent galaxies at a given M_* increases with increasing redshift. The slope and intercept of this criterion for objects at $z \sim 0.6$ is indicated in the right-hand panel of Figure 4 with a dashed line.

We show the frequency distribution of redshifts, stellar masses, and specific SFRs for these galaxies in Figure 5. In preparation for the analysis to follow in Section 7, we also compare these distributions with those for the f/g galaxies included in the QSO-galaxy pair comparison samples discussed in §2.2 (Chen et al. 2010a; Werk et al. 2013). The f/g galaxies in these samples tend to lie at lower redshifts than the PRIMUS f/g galaxies, with a median redshift $z_{\rm f/g}^{\rm QSO} = 0.23$. However, the QSO-galaxy pair and PRIMUS pair samples span a similar (and broad) range in stellar mass and specific SFR, with the median $\log M_*/M_\odot$ and $\log$sSFR values for the PRIMUS f/g galaxies in close pairs ($R_\perp < 50$ kpc) offset by -0.4 dex and $+0.6$ dex, respectively, from the median values of the comparison sample distributions. Considering only those systems lying on the star-forming sequence as defined by Eq. 1, the median $\log {\rm sSFR}/[{\rm yr}^{-1}] = -9.5$ and $\log M_*/M_\odot = 9.9$ for close PRIMUS pairs, while the QSO-galaxy star-forming pair sample has a median $\log {\rm sSFR}/[{\rm yr}^{-1}] = -10.0$ and $\log M_*/M_\odot = 10.3$. This $+0.5$ dex offset in sSFR is consistent with the "best-fit" relation between galaxy SFR, stellar mass, and age of the Universe from Speagle et al. (2014, Eq. 28), adopting $\log M_*/M_\odot = 9.9$ at age $t = 9.1$ Gyr ($z = 0.4$) and $\log M_*/M_\odot = 10.3$ at age $t = 11.0$ Gyr ($z = 0.2$). This reinforces the assertions made above and in Chen et al. (2010a) and Werk et al. (2013) that these galaxies are representative of the star-forming population at the corresponding epochs. We note that the PRIMUS pairs at $R_\perp > 50$ kpc have a median $\log M_*/M_\odot$ within $+0.15$ dex of the PRIMUS pairs having $R_\perp < 50$ kpc; however, the subsample of these wide pairs which are star-forming have a distribution of M_* which is overall lower, with median $\log M_*/M_\odot = 9.6$ and $\log {\rm sSFR}/[{\rm yr}^{-1}] = -9.5$.

6. BACKGROUND GALAXY SIZES AND MORPHOLOGIES

6.1. *Half-Light Radii*

The salient characteristics of our background galaxies are those which differentiate them from QSO sightlines: namely, their sizes and morphologies. Most germane to our analysis is the spatial distribution of sources contributing to the continuum emission of each galaxy at $\lambda_{\rm obs} \sim 3650 - 5180$ Å, or $\lambda_{\rm rest} \sim 2200 - 2700$ Å – i.e., the portion of the b/g galaxy continuum probing Mg II at $z_{\rm f/g}$. Because such sources in $z \sim 0.5 - 1$ galaxies cannot be resolved from the ground, an ideal dataset for measuring this distribution would be *HST* imaging with the ACS or WFC3/UVIS cameras in filters covering the SDSS g band (e.g., F475W).

This type of imaging is not currently available; however, those pairs located in the COSMOS fields have been deeply imaged in the ACS F814W band, sensitive to $\lambda_{\rm obs} \sim 7700 - 8400$ Å. To assess galaxy sizes in this passband, we make use of the publicly available COSMOS ACS I-band Photometry Catalog[5] (Leauthaud et al. 2007) generated using the SExtractor photometry detection software (Bertin & Arnouts 1996). From this catalog, we select measurements of half-light radii for 30 b/g galaxies which have redshifts at least 1000 km s^{-1} larger than the corresponding f/g galaxy, and for which our followup spectroscopy covers Mg II at $z_{\rm f/g}$. We then calculate the projected physical extent of these half-light radii at $z_{\rm f/g}$, $R_{\rm eff}(z_{\rm f/g})$, and show the distribution of these values in Figure 6 in black. We show the size distribution of those b/g galaxies which lack a bright broad-line AGN in cyan. To compare the sizes of these particular galaxies to the population from which they are selected, we also use the measurements in the Leauthaud et al. (2007) catalog to calculate effective radii for the ~ 1000 PRIMUS galaxies in the COSMOS field having redshifts in the range $0.4 < z^{\rm PR} < 1.0$ and having apparent B-band magnitudes $B_{\rm AB} < 22.5$. The distribution of these sizes, normalized to an arbitrary value, is shown in Figure 6 in gray.

Our PRIMUS b/g galaxies have a broad range in sizes, with the smallest object extending over only $R_{\rm eff}(z_{\rm f/g}) = 0.4$ kpc, and the largest having $R_{\rm eff}(z_{\rm f/g}) = 7.9$ kpc. Indeed, comparing the black and gray histograms, we see that the b/g galaxies include a significantly higher fraction of very compact sources than the overall bright galaxy population. However, the distribution of PRIMUS b/g galaxies without bright AGN (identified spectroscopically) is qualitatively similar to that of the broader COSMOS population: the median radii are $R_{\rm eff}(z_{\rm f/g}) = 4.1$ kpc and $R_{\rm eff}(z^{\rm PR}) = 3.9$ kpc, respectively. Furthermore, the minimum $R_{\rm eff}$ of the former (cyan) distribution is $R_{\rm eff}(z_{\rm f/g}) = 1.0$ kpc. The high surface-brightness regions of rest-frame optical emission from these systems (i.e., the inner regions producing half of the total emission) are therefore subtending projected distances (or half-light diameters) of at least ~ 2 kpc and up to $\gtrsim 8$ kpc across the halos of the corresponding f/g galaxies. And because these sizes are typical of the

[5] www.irsa.ipac.caltech.edu/data/COSMOS/datasets.html

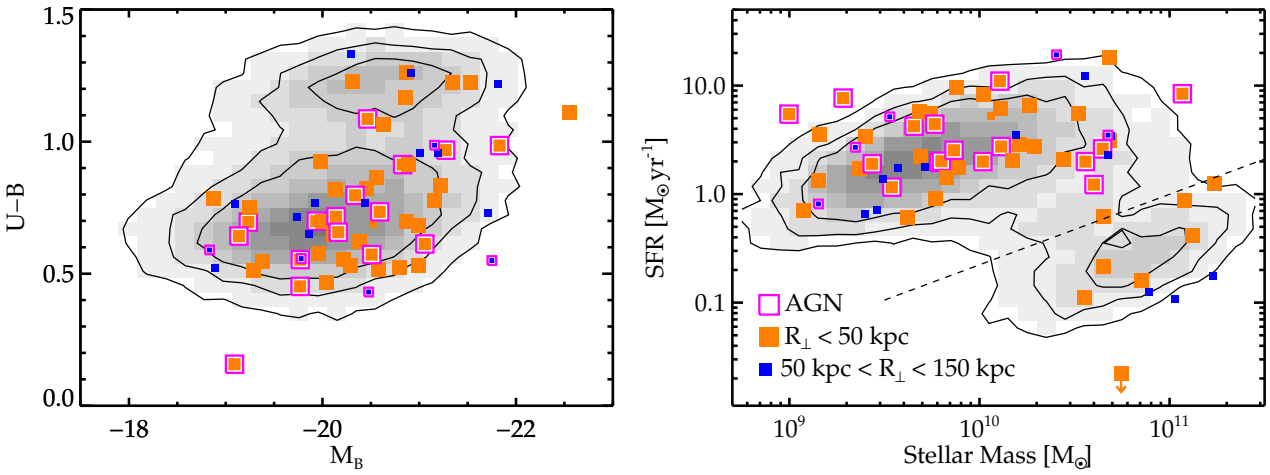

Figure 4. *Left:* $U-B$ vs. $M_{\rm B}$ for the foreground galaxies in our pair sample. Objects in pairs with $R_\perp \leq 50$ kpc are indicated with large orange squares, and objects in more widely separated pairs are marked in blue. Contours and gray shading show the $U-B$ vs. $M_{\rm B}$ distribution of all PRIMUS galaxies having $0.35 < z^{\rm PR} < 0.8$. Symbols outlined in magenta indicate pairs in which the background galaxy hosts a bright AGN. *Right:* SFR vs. stellar mass for the sample foreground galaxies. Symbol sizes and colors are consistent with those in the left-hand panel. Contours show the SFR-M_* distribution of PRIMUS galaxies at $0.35 < z^{\rm PR} < 0.8$. The dashed line indicates the dividing line between star-forming and quiescent galaxies adopted from a fit to the minimum of the galaxy distribution by Berti et al. (2016) assuming $z \sim 0.6$. A handful (7) of the f/g galaxies in our sample of close pairs has SFR $\lesssim 0.1-1\ M_\odot\ {\rm yr}^{-1}$ and occupy the "red sequence" in the color-magnitude diagram shown at left. However, the vast majority of our f/g galaxies lie along the main locus of the star-forming sequence at $z \sim 0.4-0.8$.

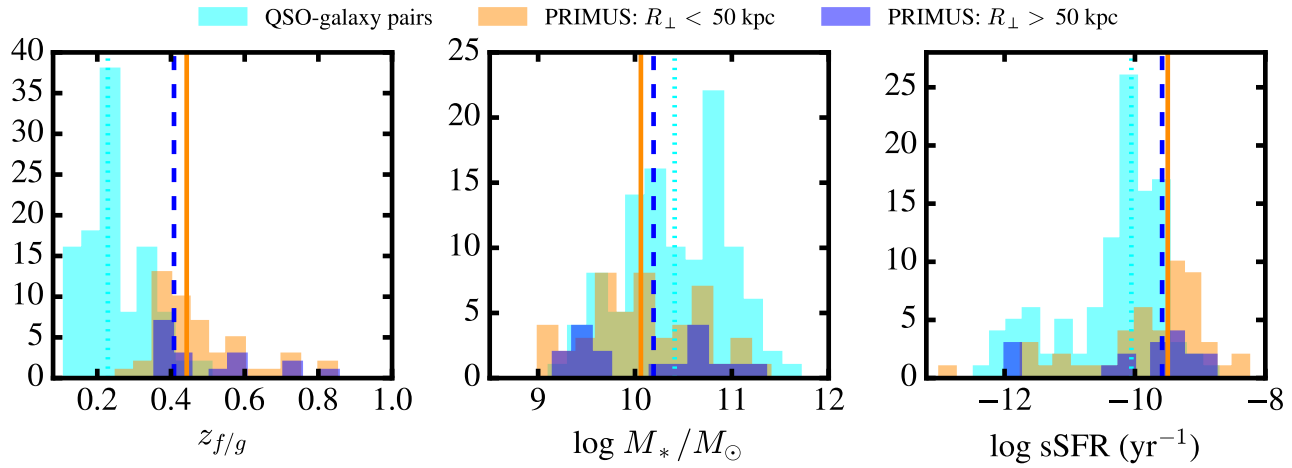

Figure 5. *Left:* Redshift distribution of our PRIMUS f/g galaxy sample. The distribution of galaxy redshifts for pairs having $R_\perp < 50$ kpc is shown in orange, with the $z_{\rm f/g}$ distribution for wider pairs shown in blue. The redshift distribution of galaxies included in the QSO-galaxy pair studies of Chen et al. (2010a) and Werk et al. (2013) is shown in cyan. The median value for each subsample is shown with a vertical line of the same color. *Middle:* Stellar mass distribution of our PRIMUS f/g galaxy sample and QSO-galaxy pair comparison samples. The colors are chosen as in the left-hand panel. *Right:* Specific SFR distribution of our PRIMUS f/g galaxy sample and QSO-galaxy pair comparison samples. The PRIMUS pairs tend to lie at higher redshifts than the comparison sample galaxies. PRIMUS pairs having $R_\perp < 50$ kpc have a median $\log M_*/M_\odot$ lower by ~ 0.4 dex and median $\log$sSFR higher by ~ 0.6 dex. The few PRIMUS pairs at $R_\perp > 50$ kpc have a median $\log M_*/M_\odot$ and median $\log$sSFR very close to that of the $R_\perp < 50$ kpc pairs.

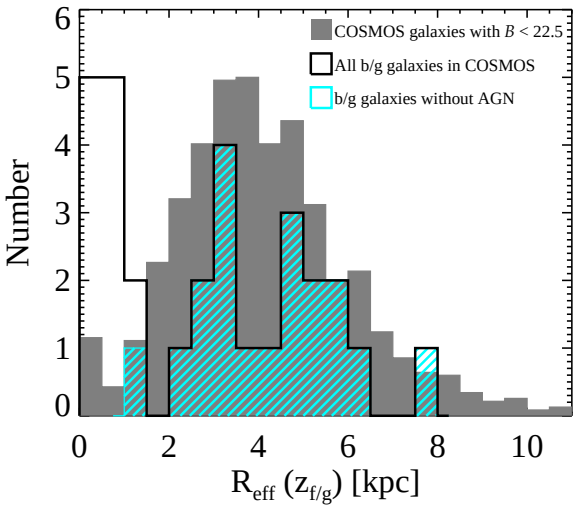

Figure 6. Distribution of half-light radii measured in *HST*/ACS F814W imaging of the b/g galaxies in our sample which are located in the COSMOS field (black). The radii are estimated at the redshift of the corresponding f/g galaxy. The distribution of sizes for those b/g galaxies without a dominant broad-line AGN is shown in cyan. The distribution of half-light radii for all galaxies in the COSMOS field having $0.4 < z^{\rm PR} < 1.0$ and $B_{\rm AB} < 22.5$ is shown in gray. These latter sizes are estimated at the redshift of the target ($z^{\rm PR}$).

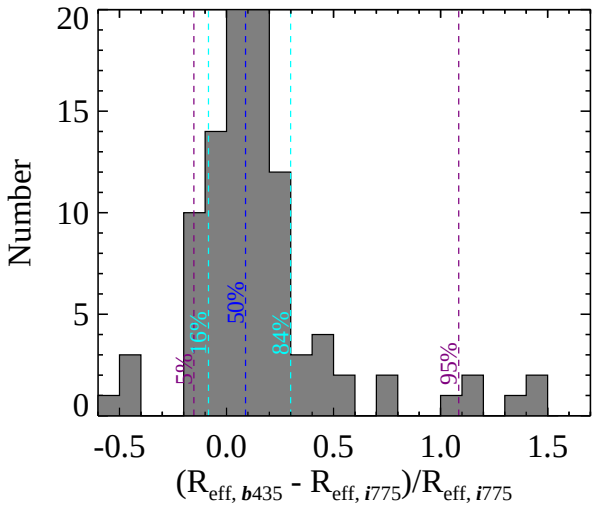

Figure 7. Distribution of the offset between half-light radii measured in the *HST*/ACS F435W and F775W filters for all galaxies observed in the Team Keck Redshift Survey (Wirth et al. 2004) to have secure redshifts in the range $0.4 < z < 1.0$ and having F435W magnitudes $b435 < 23$. The 5th, 16th, 50th, 84th, and 95th-percentile values of the distribution are marked with vertical dashed lines. The $b435$-band half-light radius is more than $\sim 12\%$ smaller than the $i775$-band half-light radius in only 5% of the galaxies.

bright ($B_{\rm AB} < 22.5$) galaxy population in the COSMOS field, we assume they are also representative of the sizes of the remainder of our b/g galaxy sample.

The rest-frame ultraviolet emission from these systems, however, may have a differing morphology. In particular, while emission at $\lambda_{\rm rest} \sim 5300$ Å includes contributions from A stars and later spectral types, $\lambda_{\rm rest} \sim 2200 - 2700$ Å emission is produced exclusively by O and B stars. To assess the distribution of offsets between half-light radii measured in the rest-frame UV vs. the rest-frame optical in a galaxy sample similar to our own, we turn to the Team Keck Redshift Survey (TKRS; Wirth et al. 2004) of the GOODS-N field (Giavalisco et al. 2004). This field has the advantage of deep imaging in both the *HST*/ACS F435W and F775W passbands and publicly-available photometry catalogs for each (Giavalisco et al. 2004). From the TKRS galaxy sample (magnitude-limited to $R_{\rm AB} < 24.4$), we select objects having $0.4 < z < 1.0$ and apparent magnitude in the F435W passband $b435 < 23.0$. We then calculate the relative offset in the half-light radii measured for each galaxy in the F435W and F775W bands, $(R_{{\rm eff},b435} - R_{{\rm eff},i775})/R_{{\rm eff},i775}$. The distribution of this quantity is shown in Figure 7. The median value of this distribution is $\sim +0.09$, indicating that $R_{{\rm eff},b435}$ is typically $\sim 10\%$ larger than $R_{{\rm eff},i775}$. Indeed, $R_{{\rm eff},b435}$ is $\sim 15\%$ *smaller* than $R_{{\rm eff},i775}$ only below the 5th-percentile value of the distribution. This suggests that the b/g galaxy sizes we measure in the F814W *HST*/ACS passband (Figure 6) are similar to the sizes of the beams produced by their $\lambda_{\rm rest} \sim 2200 - 2700$ Å emission.

6.2. *The Detailed Distribution of Rest-Frame UV Continuum Emission*

A significant fraction of the young O and B stars which are producing continuum emission in the UV are known to form in embedded clusters within molecular clouds (Lada & Lada 2003). Stellar winds and radiation from these clusters are expected to disrupt and destroy the remainder of their nascent clouds within a few Myr (Murray et al. 2010). Because these young, bright clusters are likely to survive disruption by, e.g., stellar mass loss or tidal disturbances for at least $\gtrsim 10^7 - 10^8$ yr (Fall et al. 2009), the integrated (but instantaneous) UV emission from a star-forming galaxy may therefore be dominated by light from massive star clusters. In the context of intervening absorption studies, because young clusters have radii of only $r_{cl} \sim 0.1 - 10$ pc (Lada & Lada 2003; Murray et al. 2010), b/g galaxies may be viewed as a closely-spaced set of numerous pencil-beam sightlines. A recent survey of the young cluster population of lo-

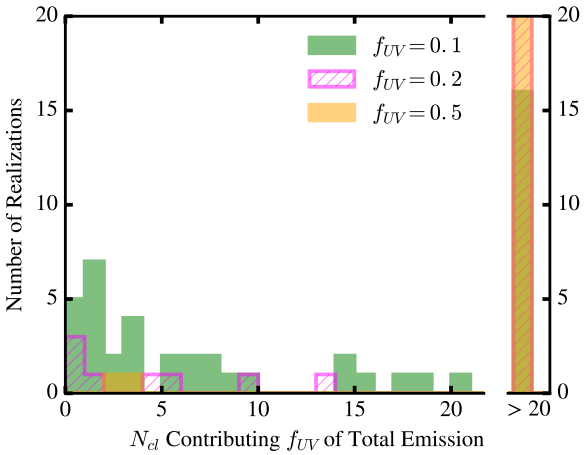

Figure 8. The distribution of the number of clusters ($N_{\rm cl}$) which emit up to a set fraction ($f_{\rm UV}$) of the total $L_{\rm tot}^{\rm F225W}$ of a given SLUG galaxy realization. Realizations for which the number of clusters producing the assigned $f_{\rm UV}$ exceeds 20 are indicated in the right-most bin. For $f_{\rm UV} = 0.2$ (magenta) and 0.5 (orange), the number of clusters producing $f_{\rm UV} \times L_{\rm tot}^{\rm F225W}$ exceeds 20 in nearly all realizations, such that the height of the right-most bin exceeds the range of the y-axis. It is somewhat more common for just a handful of clusters to contribute only a fraction $f_{\rm UV} = 0.1$ of the total $L_{\rm tot}^{\rm F225W}$ (green histogram).

cal star-forming galaxies indicates that massive spirals may host several hundred or more than 1000 individual clusters (Krumholz et al. 2015b; Grasha et al. 2015); however, for our purposes, it is of interest to consider in particular the total number of such clusters which make a dominant contribution to the rest-frame UV continuum. For instance, in the extreme case that a galaxy's UV light is dominated by only a single massive young cluster, the b/g beam of that galaxy would have a morphology similar to that of a QSO. While this scenario is unlikely in view of our finding that the half-light radii of $z \sim 0.4 - 1.0$ galaxies is similar at both $\lambda_{\rm obs} \sim 4400$ Å and $\lambda_{\rm obs} \sim 7750$ Å, if it were to arise it would weaken our experimental leverage on the sizes of f/g absorbers.

To estimate the number and luminosity of young clusters in a "typical" b/g galaxy at the epoch of observation, we make use of the SLUG stellar population synthesis code[6] (da Silva et al. 2012; Krumholz et al. 2015a). SLUG predicts the spectrum of a given stellar population with an explicit accounting for the stochastic nature of star and star cluster formation. Rather than adopting initial mass functions, cluster mass functions, star formation histories, etc., which are constant in time, SLUG assigns each of these relations a probability distribution function. To simulate the growth of a galaxy, the user must first select the fraction (f_c) of stars which are expected to form in clusters (as opposed to the field). SLUG then calculates the total mass in stars which must be formed at a given time step as set by the star formation history. The code draws cluster masses from the input cluster mass function until it has formed the appropriate amount of mass in clusters. It then populates each cluster with stars by drawing from the initial mass function probability distribution. The stars are allowed to age over time, and the clusters are also disrupted (and join the field population) on a time scale drawn from the specified cluster lifetime function.

At each timestep, SLUG computes the composite spectrum of all stars in the simulation, as well as the spectrum of each individual star cluster. In addition, the code package includes throughput curves for numerous filters, allowing the user to calculate the total luminosity of the system as well as the luminosity of individual clusters in several passbands in common use. We simulate a galaxy with a continuous star formation rate of 0.1 $M_\odot$ yr^{-1} and with the fraction f_c set to 1 (i.e., such that all stars form in clusters) for a total of 200 Myr. We adopt the default settings specified in SLUG for the remaining simulation inputs, including a Chabrier IMF (Chabrier 2005), a cluster mass function $dN_{cl}/dM_{cl} \propto M_{cl}^{-2}$, and a cluster lifetime function $dN_{cl}/dt \propto t^{-1.9}$. We then generate 48 realizations of this simulation, recording the luminosity of each galaxy and each individual cluster in the F225W filter available with the *HST*/WFC3 UVIS channel in the galaxy's rest frame. This filter has an effective wavelength $\lambda_{\rm eff} \sim 2359$ Å and a width of 467 Å, and thus samples the spectral window of interest.

At the final time step of each realization, we rank order the clusters by their F225W luminosity ($L_{\rm cl}^{\rm F225W}$). We then calculate the cumulative luminosity of the clusters at each rank position, and divide this luminosity by the total integral F225W luminosity of the system ($L_{\rm tot}^{\rm F225W}$). Using these cumulative distributions, we then count the number of clusters which emit some fraction, $f_{\rm UV}$, of the total $L_{\rm tot}^{\rm F225W}$ in each realization. Figure 8 shows the distribution of these cluster counts for three values of $f_{\rm UV} = 0.1, 0.2$, and 0.5 (in green, magenta, and orange, respectively). In about half of our galaxy realizations, at least 10% of the total $L_{\rm tot}^{\rm F225W}$ is produced by fewer than 10 clusters (see the green histogram). Indeed, in five realizations, the brightest cluster produces *more* than 10% of $L_{\rm tot}^{\rm F225W}$. However, it is unusual for

[6] http://slug2.readthedocs.io/en/latest/intro.html

fewer than 10 clusters to produce more than 20% of the total UV emission from each simulation (magenta histogram), and fewer than 10 clusters produce more than half of $L_{\rm tot}^{\rm F225W}$ in only two realizations (orange histogram). This demonstrates that the UV continuum emission from such systems is not dominated by only a handful of bright sources, but instead is generated in approximately equal measure by many tens or hundreds of star clusters.

We have used SLUG to verify that the number of these realizations that are dominated by a few bright clusters decreases with increasing SFR. This strongly suggests that our bright, blue b/g galaxy sample is less likely to be dominated by only a few bright clusters than implied by Figure 8. Furthermore, if we relax our assumption of a constant SFR, we find that we produce model galaxies which are indeed dominated by a handful of bright star clusters only if they are observed very close to the onset of a burst of star formation. For instance, for models with an exponentially-decaying starburst with a decay time = 10 Myr (and which produce a mean SFR of 0.1 $M_\odot$ yr^{-1} over 100 Myr), approximately two-thirds of the model realizations yield UV continuum emission which is dominated (at the $>50\%$ level) by fewer than 10 clusters if they are observed within 20 Myr of the burst onset. At later times (i.e., within ≥ 40 Myr), these clusters have aged or have been disrupted, such that only $<10\%$ of realizations remain dominated by individual clusters to this extent. Given this very short timescale, it is unlikely that our b/g galaxy sample is composed primarily of objects in such a cluster-dominated phase.

In what follows, we will use this analysis to bolster our assumption that the UV continuum beams provided by our b/g galaxy sample are made up of numerous point sources with a similar spatial extent as is measured in the F814W band (i.e., in Figure 6). This will inform our interpretation of our absorption line analysis as discussed in §7 and in Paper II.

7. THE MG II-ABSORBING CGM AS PROBED BY PRIMUS GALAXIES

7.1. *The W_{2796}-$R_\perp$ Relation*

Figure 9 shows our constraints on W_{2796} measured around each of the sample f/g galaxies as a function of the pair projected separation ($R_\perp$). Pairs with $R_\perp < 50$ kpc are indicated with large orange squares, and pairs with larger impact parameters are shown with dark blue squares. Symbols for pairs in which the b/g galaxy is host to a bright QSO or broad-line AGN are outlined in magenta. It is those pairs without this indication that have b/g sightlines which are not dominated by a bright nuclear source (see Figure 6), and hence which may be considered to offer a truly novel (i.e., spatially-extended) probe of f/g absorption. W_{2796} measurements for which the $\pm1\sigma$ uncertainty interval extends to < 0.05 Å are shown as 2σ upper limits. Fifteen of our securely-detected absorbers have $W_{2796} > 1.0$ Å; ~ 6 of these absorbers exhibit $W_{2796} > 2$ Å. Furthermore, we are approximately equally likely to detect such strong absorbers toward non-AGN hosts as we are toward bright AGN. The overall sensitivity of our survey is lower than that of the QSO-galaxy comparison samples, such that a number of our b/g sightlines yield quite weak upper limits on W_{2796}. However, while the b/g QSOs in our sample provide the most constraining W_{2796} limits (at ~ 0.15 Å), we are able to place limits as low as ~ 0.3 Å using a few of our non-AGN host b/g objects.

Numerous QSO-galaxy pair studies have noted a decline in W_{2796} with increasing $R_\perp$ at high statistical significance (e.g., Lanzetta & Bowen 1990; Steidel 1995; Kacprzak et al. 2008; Chen et al. 2010a; Nielsen et al. 2013). To characterize the relation between W_{2796} and $R_\perp$ in our sample, we model our dataset assuming a linear dependence of $\log W_{2796}$ on $R_\perp$ as described by Nielsen et al. (2013):

$$\log W_{2796} = b + m_1 R_\perp. \tag{2}$$

Following the methodology of Chen et al. (2010a), the likelihood function for this model can be written

$$\mathcal{L}(\overline{W}) = \left(\prod_{i=1}^{n} \frac{1}{\sqrt{2\pi s_i^2}} \exp\left\{ -\frac{1}{2} \left[\frac{W_i - \overline{W}}{s_i} \right]^2 \right\} \right) \times \left(\prod_{i=1}^{m} \int_{-\infty}^{W_i} \frac{dW'}{\sqrt{2\pi s_i^2}} \exp\left\{ -\frac{1}{2} \left[\frac{W' - \overline{W}}{s_i} \right]^2 \right\} \right),$$

with W_i representing the $\log W_{2796}$ value for each measurement i, and $\overline{W}$ equal to the value of $\log W_{2796}$ given by the model at each $R_{\perp,i}$. The first product includes all n systems which yield a direct measurement of $\log W_{2796}$, and the second includes the m systems for which our constraint on $\log W_{2796}$ is an upper limit. We assume that the Gaussian variance in this expression has two components:

$$s_i^2 = \sigma_i^2 + \sigma_C^2, \tag{3}$$

with σ_i representing the measurement uncertainty in $W_{2796,i}$, and σ_C an additional factor which accounts for intrinsic scatter in the relation.[7] Hence, because we are making the assumption that the dispersion in the

[7] This follows the recommendations for model fitting offered in the online documentation for the `emcee` software package at http://dan.iel.fm/emcee/current/user/line/.

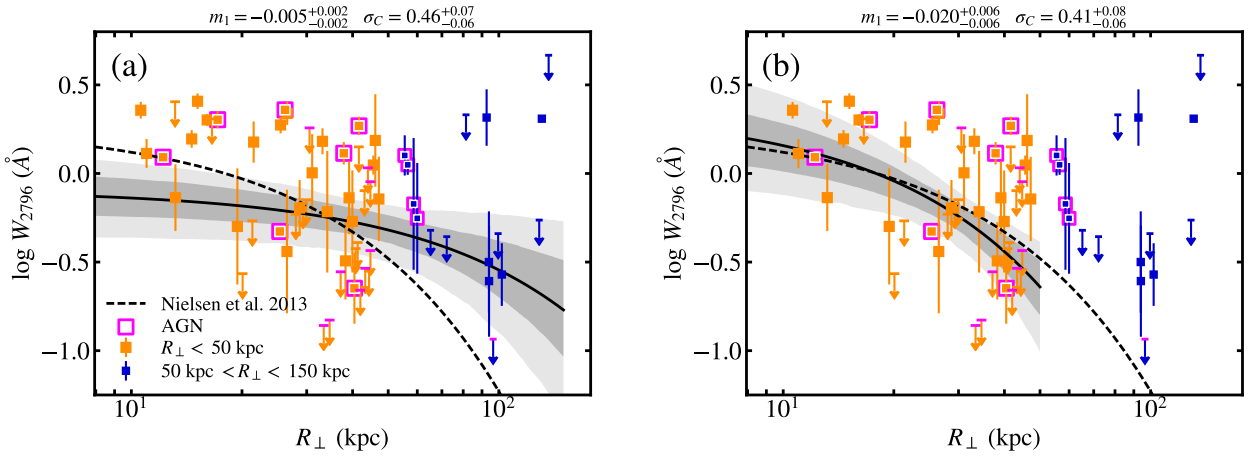

Figure 9. *(a)* W_{2796} measured along PRIMUS b/g galaxy sightlines vs. projected distance $R_\perp$ from the associated f/g galaxies. The symbol colors and sizes match those used in Figures 3 and 4. Symbols outlined in magenta indicate pairs in which the background galaxy hosts a bright AGN. The solid black line shows the "best-fit" linear relation between $\log W_{2796}$ and $R_\perp$ determined as described in Section 7.1 for the full dataset. The dark and light gray contours indicate the locus of curves with slopes and intercepts drawn from the inner ±34% and ±47.5% of the PPDFs of each model parameter. The best-fit values of the slope (m_1) and intrinsic scatter (σ_C) and their uncertainty intervals are printed above the plot. The dashed black curve shows the log-linear fit to the QSO-galaxy pair Magiicat dataset from Nielsen et al. (2013). *(b)* The W_{2796} measurements and Nielsen et al. (2013) relation are the same as shown in panel *(a)*. Here, the solid black line and dark and light gray contours show the best-fit relation between $\log W_{2796}$ and $R_\perp$ and the analogous uncertainty intervals for measurements with $R_\perp < 50$ kpc.

quantity $\log W_{2796}$ is Gaussian, we are equivalently assuming that the scatter in W_{2796} is lognormal. While this assumption is not unreasonable, we caution that the number of measurements in both our PRIMUS pair and QSO-comparison datasets is insufficient to perform a test with the power to rule out this claim (i.e., to constrain the shape of the $\log W_{2796}$ distribution over a narrow range in $R_\perp$).

We sample the posterior probability density function (PPDF) for this model using the Markov Chain Monte Carlo technique as implemented in the Python software package `emcee`, an open source code which uses an affine-invariant ensemble sampler (Foreman-Mackey et al. 2013). We adopt uniform probability densities over the intervals $-5.0 < m_1 < 5.0$, $-10.0 < b < 10.0$, and $-10.0 < \ln \sigma_C < 10.0$ as priors. We find that Markov chains generated by 100 "walkers" each taking 6000 steps (and discarding the first 1000 steps) provide a thorough sampling of the PPDF in each parameter dimension. The code outputs the parameter values with maximum likelihood, as well as marginalized PPDFs. In the following, we adopt the median and ±34th-percentiles of these PPDFs as the "best" value of each parameter and its uncertainty interval.

The results of this procedure are shown in Figure 9. Panel *(a)* shows the best-fit relation between $R_\perp$ and $\log W_{2796}$ for all the datapoints plotted (i.e., for 0 kpc $< R_\perp <$ 150 kpc). The dark and light gray contours were obtained by first selecting 1000 sets of parameter values from the PPDF at random, determining the corresponding $\overline{W}$ values for each parameter set, and then filling in the region of the figure containing the inner ±34% and ±47.5% of $\overline{W}$ values at each point along the x-axis. This relation is quite flat, with a slope of only $m_1 = -0.004 \pm 0.002$, an intercept $b = -0.09^{+0.12}_{-0.12}$, and an intrinsic scatter $\sigma_C = 0.46^{+0.07}_{-0.06}$. Such a flat slope is in fact inconsistent with the log-linear fit to the Magiicat dataset over a similar range in $R_\perp$ (5 kpc $< R_\perp <$ 200 kpc) presented in Nielsen et al. (2013, with $m_1 = -0.015 \pm 0.002$ and $b = 0.27 \pm 0.11$; dashed line in Figure 9).

A by-eye comparison of the distribution of the points in the figure and the locus of the Nielsen et al. (2013) relation suggests that the PRIMUS pair dataset may be offset to higher W_{2796} at high impact parameters in particular; and furthermore, that it is these high W_{2796} values at large $R_\perp$ which tend to flatten the best-fit slope. Restricting our fitting procedure to the measurements within $R_\perp < 50$ kpc (i.e., to the region of parameter space over which our sampling is most thorough), we show the resulting best fit and corresponding uncertainty intervals with a solid black line and gray contours in Figure 9b. This yields a somewhat steeper relation, consistent with that of Nielsen

et al. (2013), with $m_1 = -0.020 \pm 0.006$, an intercept $b = 0.36 \pm 0.19$, and $\sigma_C = 0.41^{+0.08}_{-0.06}$. We note that whereas Nielsen et al. (2013) limited their f/g galaxy sample to include only "isolated" objects (i.e., objects without a neighbor within 100 kpc and having a velocity separation of < 500 km s^{-1}), the PRIMUS pair sample is not restricted based on environment. Indeed, Chen et al. (2010a) found that W_{2796} exhibits no significant trend with increasing $R_\perp$ around galaxies within group environments, suggesting that a simultaneous fit to $\log W_{2796}$ vs. $R_\perp$ including both isolated and group f/g galaxies would yield a flatter relation than that reported by Nielsen et al. (2013). At the same time, however, the strongest absorber among the eight sightlines probing group environments in the Chen et al. (2010a) sample has $W_{2796} = 0.79 \pm 0.03$ – i.e., well below several of the PRIMUS f/g absorbers at $R_\perp > 50$ kpc.

7.2. *The Relation Between W_{2796} and Intrinsic Host Galaxy Properties*

We now test our sample for additional correlations between W_{2796} and intrinsic host galaxy properties (e.g., M_*, SFR, and sSFR) at fixed values of $R_\perp$. Such correlations have been noted in several studies, beginning with Chen et al. (2010b). These authors found that the scatter in the relation between $\log W_{2796}$ and $\log R_\perp$ is reduced when additional terms which scale linearly with $\log M_*$ and log sSFR are included. More recently, using a larger QSO-galaxy pair sample (including both absorption-selected galaxies and pairs selected without prior knowledge of the presence of halo Mg II absorption), Nielsen et al. (2013) presented strong evidence for an increase in W_{2796} with increasing host galaxy B- and K-band luminosity at fixed $R_\perp$, and further reported a weak dependence of W_{2796} on galaxy color of marginal statistical significance. Churchill et al. (2013), in their discussion of the same dataset, interpreted these results as indicative of a positive scaling between W_{2796} and the virial mass of the host halo at fixed $R_\perp$. Lan et al. (2014) additionally reported that relative to all galaxies within $R_\perp < 50$ kpc of Mg II absorbers, those with higher SFR and sSFR are associated with increasingly enhanced excess W_{2796}. They further drew a distinction between star-forming and quiescent host galaxies, finding that while this excess W_{2796} tends to increase with the M_* of star-forming galaxies, quiescent galaxies do not give rise to a significant W_{2796} excess regardless of their M_* (within $R_\perp < 50$ kpc). And at higher redshifts ($z \sim 2$), discovery of the high incidence and absorption strength in low-ionization metal transitions measured in the massive halos of QSO host galaxies has likewise pointed to a positive correlation between cool gas absorption strength and halo mass, at least among the active star-forming and QSO hosts which have been studied at such early epochs (Prochaska et al. 2013a, 2014).

We approach a test for such correlations by comparing the cumulative distributions of W_{2796} values among subsamples of sightlines in our survey. First, we isolate the handful of sightlines (~ 7) which probe quiescent galaxy halos, defined as described by Eq. 1. To control for the possible effect of galaxy quiescence, and because there are relatively few of these sightlines in our sample, we exclude them from all cumulative distributions described below. We then subdivide our sample into two bins with $R_\perp < 30$ kpc and 30 kpc $< R_\perp < 50$ kpc as shown in Figure 10a with black open and gray filled points, respectively. In Figure 10b, we show the cumulative distribution ($F(\log W_{2796} > \log W^0_{2796})$) of $\log W_{2796}$ (i.e., the fraction of systems having $\log W_{2796}$ greater than a given value $\log W^0_{2796}$) for sightlines having $R_\perp < 30$ kpc (black open histogram) and for those at 30 kpc $< R_\perp < 50$ kpc (gray filled histogram). All upper limits on W_{2796} are included in these distributions at their 2σ values if they are < 0.5 Å; weaker limits are excluded, as they may have the effect of inflating $F(\log W_{2796} > \log W^0_{2796})$ at large W_{2796} relative to the $F(\log W_{2796} > \log W^0_{2796})$ measured in a more sensitive spectroscopic survey.

It is evident from Figure 10b that the cumulative distribution within $R_\perp < 30$ kpc includes a higher frequency of large W_{2796} values relative to the $F(\log W_{2796} > \log W^0_{2796})$ at larger impact parameters. We test the statistical significance of this offset using `ASURV` Rev 1.2 (Lavalley et al. 1992), a software package designed for statistical analysis of censored data invoking methods presented in Feigelson & Nelson (1985). Using `ASURV`, we perform a Gehan's generalized Wilcoxon test of the probability that these two W_{2796} distributions are drawn from the same parent population. Here, we do not exclude any upper limits on W_{2796}, regardless of their value, as `ASURV` properly accounts for the weighting of censored data. The results of this test, along with the number of sightlines and the median W_{2796} in each subsample, are included in the first column of data in Table 5. The median W_{2796} value is nearly 1 Å higher for sightlines within 30 kpc relative to sightlines at 30 kpc $< R_\perp < 50$ kpc, and the probability that these distributions are drawn from the same parent population is only $P = 0.003$. This result is unsurprising, and is fully consistent with the findings of §7.1.

We next further subdivide each of the samples described above by the M_*, SFR, and sSFR of the as-

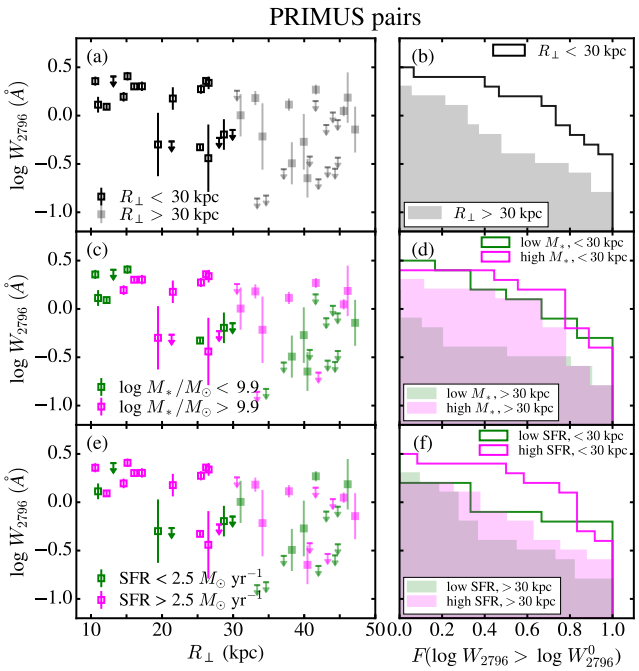

Figure 10. *(a)* $\log W_{2796}$ vs. projected distance $R_\perp$ measured along PRIMUS b/g sightlines probing star-forming f/g halos. Sightlines within $R_\perp < 30$ kpc and at 30 kpc $< R_\perp <$ 50 kpc are indicated with open black and filled gray symbols, respectively. *(b)* Cumulative distribution of $\log W_{2796}$ in each subsample shown in panel *(a)*. The x-axis value indicates the fraction of sightlines having $\log W_{2796}$ greater than the y-axis value within $R_\perp < 30$ kpc (open black histogram) and with 30 kpc $< R_\perp < 50$ kpc (filled gray histogram). *(c)* The identical $\log W_{2796}$ vs. $R_\perp$ distribution shown in panel *(a)*, with the point color indicating f/g galaxies with $\log M_*/M_\odot < 9.9$ (green) and $\log M_*/M_\odot > 9.9$ (magenta). Panel *(d)* shows the cumulative distributions of $\log W_{2796}$ for these low- and high-M_* subsamples at $R_\perp < 30$ kpc (open green and magenta histograms) and at 30 kpc $< R_\perp < 50$ kpc (filled green and magenta histograms). Panel *(e)* shows the same measurements once again, here with the datapoints color-coded according to the SFR of the f/g galaxy as indicated in the legend. *(f)* Cumulative distributions of $\log W_{2796}$ for these low- and high-SFR subsamples as described above. Upper limits on W_{2796} are included in all cumulative distributions at their 2σ values if they are < 0.5 Å. All other limits are excluded. Sightlines passing close to higher-M_* galaxies tend to yield higher W_{2796}, particularly at 30 kpc $< R_\perp <$ 50 kpc. Larger W_{2796} values also tend to arise around host galaxies with higher SFR.

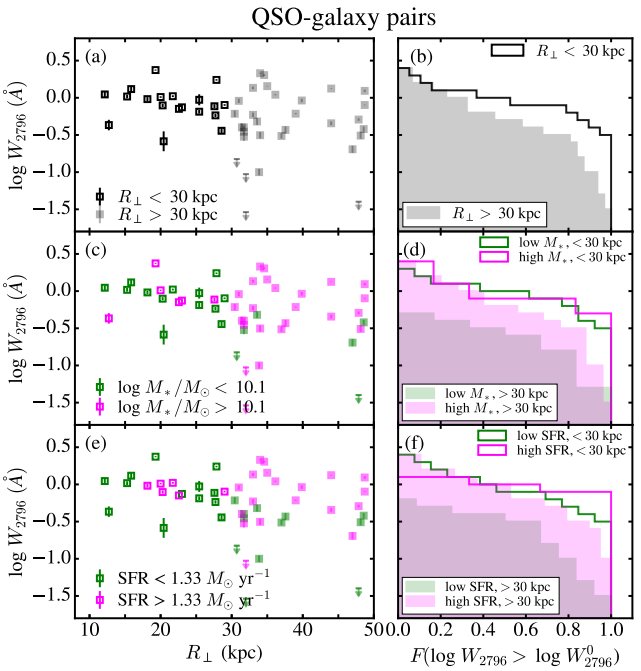

Figure 11. Same as Figure 10, for our QSO-galaxy comparison dataset adopted from Chen et al. (2010a) and Werk et al. (2013). Here we use slightly different values of $\log M_*/M_\odot$ and SFR to subdivide the sample in panels *(c)*, *(d)*, *(e)*, and *(f)* as indicated in the legends.

sociated f/g galaxies, again excluding any quiescent systems. Figure 10c includes the same measurements plotted in panel *(a)*, here with green symbols indicating sightlines probing the halos of f/g galaxies having $\log M_*/M_\odot < 9.9$, and with magenta symbols indicating sightlines probing higher-M_* systems. Figure 10d shows $F(\log W_{2796} > \log W^0_{2796})$ for each of these subsamples: those with $R_\perp < 30$ kpc are shown with green and magenta open histograms, and the subsamples at 30 kpc $< R_\perp < 50$ kpc are shown with green and magenta filled histograms. The cumulative distributions for the two subsamples at small impact parameters appear similar, and our statistical test ($P = 0.892$) fails to rule out the null hypothesis that they are drawn from different parent populations (Table 5). At 30 kpc $< R_\perp < 50$ kpc, however, there is a very low probability ($P = 0.006$) that the subsamples divided by M_* are drawn from the same distribution, with the high-M_* subsample exhibiting a median $W_{2796} \sim 0.9$ Å above that of the low-M_* subsample. We then repeat this analysis, instead subdividing the samples at SFR $= 2.5\ M_\odot$ yr^{-1}, and show the resulting scatterplot and cumulative distributions in Figure 10 panels *(e)* and *(f)*. We find that in general, subsamples probing higher-SFR f/g galaxy halos tend to exhibit higher W_{2796}, but that the probability of the low- and high-SFR subsamples originating from the same distribution rules out the null hypothesis only within $R_\perp < 30$ kpc ($P = 0.049$). Finally, we subdivide the $R_\perp < 30$ kpc and 30 kpc $< R_\perp < 50$ kpc subsamples by sSFR at $\log \mathrm{sSFR}\ [\mathrm{yr}^{-1}] = -9.46$, finding that the corresponding cumulative distributions appear similar in both impact parameter bins, and finding no

evidence suggesting their parent populations are distinct (see Table 5).

Broadly speaking, we see evidence for larger-W_{2796} systems associated with host galaxies with higher M_* or SFR. This trend is not statistically significant in every $R_\perp$ bin tested; however, we consider our results to be qualitatively similar to those reported in the studies described above, as our relatively small sample size and low-S/N spectroscopy cannot rule out the persistence of these relationships over a wider range in $R_\perp$. To more directly test for consistency with previous work, however, we now perform the same analysis laid out above on the QSO-galaxy comparison sample described in §5. In Figure 11, we show the W_{2796} vs. $R_\perp$ distributions and cumulative distribution of W_{2796} values in this comparison sample in subsamples divided by $R_\perp$ (panels *(a)* and *(b)*), M_* (panels *(c)* and *(d)*), and SFR (panels *(e)* and *(f)*). Here, we have excluded sightlines probing quiescent galaxies defined as in Eq. 1. We treat upper limits on W_{2796} as described above; in practice, all upper limits are included in these distributions, as the QSO spectroscopy tends to be much more sensitive than our b/g galaxy spectroscopy. We also adopt slightly different values for the M_* and SFR at which we split these subsamples, adjusting our divisions so that there are at least 5 objects in each. The specific values chosen are indicated in the legends in Figure 11. For completeness, we also subdivide this sample by sSFR, and show the results of our tests for consistency among the corresponding cumulative distributions in Table 5.

We do not rule out consistency between the distributions of W_{2796} in these QSO sightlines at impact parameters < 30 kpc when dividing the sample by M_* or SFR. At 30 kpc $< R_\perp <$ 50 kpc, however, the median W_{2796} of the high-M_* and high-SFR subsamples are ~ 0.4 Å higher than in the low-M_* and SFR subsamples, and there is a very low probability that these subsets are drawn from the same parent population ($P < 0.02$). We find no evidence for significant differences between the subsamples divided by sSFR.

These findings are fully consistent with those reported above for the PRIMUS subsamples divided both by M_* and sSFR. We note that the PRIMUS subsamples divided by SFR yield somewhat different results: we fail to rule out the null hypothesis for low- vs. high-SFR PRIMUS f/g galaxies at 30 kpc $< R_\perp <$ 50 kpc, and rule it out at $\sim 2\sigma$ significance at $R_\perp < 30$ kpc. It is possible that this discrepancy is due to the differences in background beam sizes used to probe the PRIMUS vs. QSO-galaxy f/g samples; however, given the overall agreement between all other two-sample test results, we argue that this discrepancy is more likely due to differences in the SFR distributions of the two samples and/or to the large uncertainties in our SFR estimates (i.e., relative to the uncertainties associated with our estimates of M_*.)

All together, the foregoing analysis of both the PRIMUS and QSO-galaxy pair samples points to an increase in W_{2796} with both M_* and SFR. Although this dependence is not found to be statistically significant in both impact parameter bins studied, we consider our findings to further demonstrate a qualitative consistency between the trends in the W_{2796} distributions observed toward b/g QSOs and b/g galaxies.

7.3. *Comparison between Galaxy-Galaxy and QSO-Galaxy Samples*

We also note, however, that the PRIMUS sightline subsample within $R_\perp < 30$ kpc exhibits a median $W_{2796} = 1.3$ Å, ~ 0.5 Å higher than the analogous QSO-galaxy comparison sightline sample. To investigate the possible origin of this offset, in Figure 12 we examine the distributions of M_* (top row) and SFR (bottom row) in the $R_\perp < 30$ kpc (left column) and 30 kpc $< R_\perp <$ 50 kpc (middle column) subsamples discussed above. The same distributions for sightlines at 50 kpc $< R_\perp <$ 150 kpc are shown for completeness in the right-most column. The combined open/filled orange histograms show these distributions for all star-forming f/g galaxies in PRIMUS, while the combined open/filled cyan histograms include all star-forming f/g galaxies in the QSO-galaxy comparison sample. Comparing these distributions in the left-hand column, we see that the PRIMUS f/g galaxy sample includes a few objects with $\log M_*/M_\odot > 10.5$, while the stellar masses in the QSO-galaxy sample do not exceed this limit. The QSO-galaxy sample also has SFRs which are lower overall by $\gtrsim 0.5$ dex. The evidence presented in §7.2 for larger W_{2796} around f/g galaxies of higher M_* and/or SFR suggests that the higher median W_{2796} measured around the PRIMUS f/g galaxies may indeed be due to the larger stellar masses or SFRs of this subsample. Alternatively, these offsets could in principle also arise from the differences in the sizes of the b/g beams used in the two studies. Here, we test the former hypothesis; however, we will return to the potential effects of b/g beam size on the W_{2796} distribution of f/g absorbers in Paper II.

At 30 kpc $< R_\perp <$ 50 kpc (middle column), the PRIMUS f/g galaxies tend to have slightly lower M_* values than their counterparts in the QSO-galaxy sample, but occupy a comparable range in SFR. Indeed, their median W_{2796} values are similar (0.27 Å vs. 0.43 Å; see Table 5). However, to test for full consistency

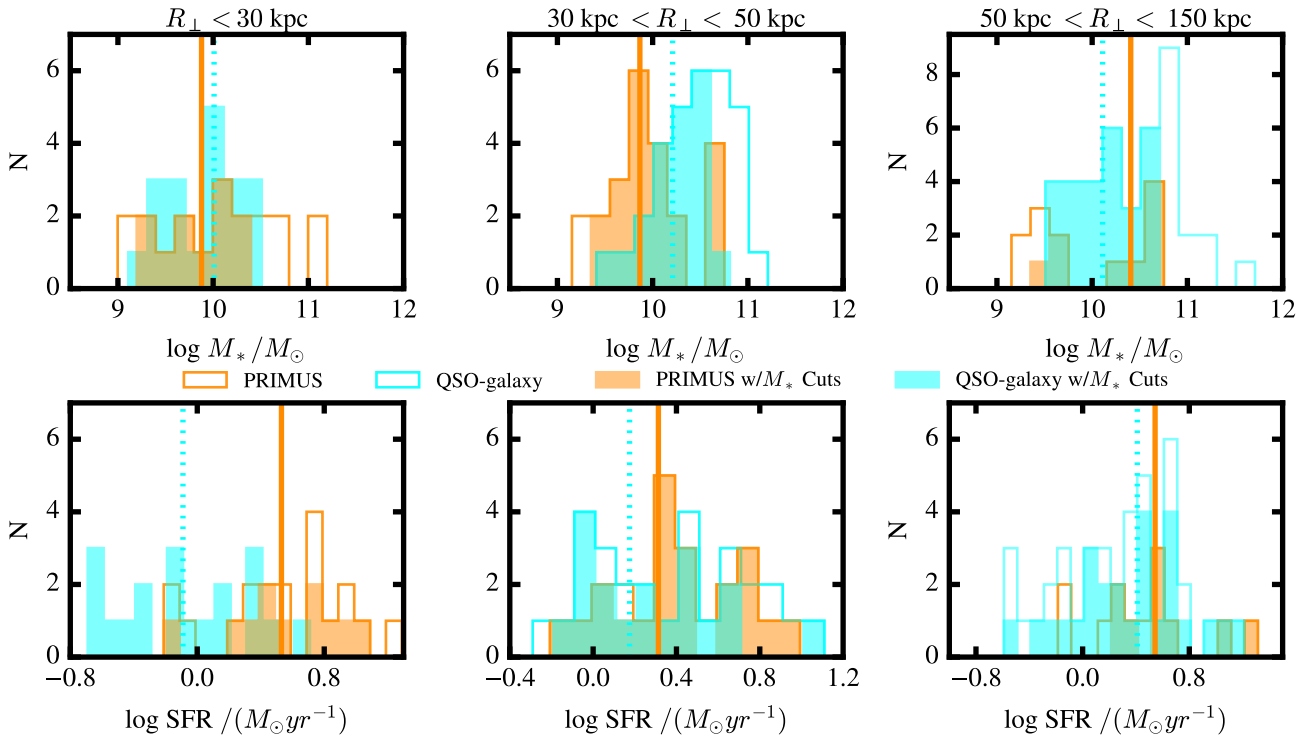

Figure 12. *Top Row:* The distribution of M_* for all star-forming f/g galaxies in PRIMUS (orange open and filled histograms) and in the QSO-galaxy comparison sample (cyan open and filled histograms) within $R_\perp < 30$ kpc (left), with 30 kpc $< R_\perp <$ 50 kpc (middle), and with 50 kpc $< R_\perp <$ 150 kpc (right). The filled portion of each histogram shows systems we select for comparison between the two samples (such that they span the same ranges in M_* in each impact parameter bin). The median value of each filled histogram is shown with a vertical curve of the same color. *Bottom Row:* The distribution of SFR for each subsample shown in the top row. The median values are indicated with vertical curves as above. The SFRs of the f/g galaxies in the QSO-galaxy comparison sample tend to be much lower (~ 0.6 dex in the median) than in our PRIMUS sample at $R_\perp < 30$ kpc. At 30 kpc $< R_\perp <$ 50 kpc these SFRs have similar distributions.

between these samples, we now select subsets of the distributions shown in Figure 12 for a more detailed comparison. At small impact parameters ($R_\perp < 30$ kpc), we exclude galaxies from the PRIMUS sample which have M_* outside the range spanned by the QSO-galaxy comparison sample; i.e., we exclude galaxies with $\log M_*/M_\odot < 9.1$ or $\log M_*/M_\odot > 10.4$. Those galaxies which remain are included in the filled orange histograms. At larger impact parameters (30 kpc $< R_\perp <$ 50 kpc), we exclude PRIMUS galaxies with stellar masses lower than the least massive galaxy in the QSO-galaxy comparison sample ($\log M_*/M_\odot < 9.4$; filled orange histograms). We also remove QSO-galaxy pairs with f/g masses higher than the most massive PRIMUS galaxy in this bin ($\log M_*/M_\odot > 10.7$; filled cyan histograms). Finally, for a complete comparison, we select a subsample of PRIMUS sightlines at 50 kpc $< R_\perp <$ 150 kpc with f/g galaxies within the stellar mass range spanned by the QSO-galaxy comparison sample ($9.5 < \log M_*/M_\odot < 11.6$), and refine this QSO-galaxy subsample by removing objects with $\log M_*/M_\odot > 10.7$.

The median values of each of these trimmed sample distributions are indicated with vertical lines. The median stellar masses of the modified samples are very similar, and the median SFRs are within < 0.2 dex at 30 kpc $< R_\perp <$ 50 kpc and 50 kpc $< R_\perp <$ 150 kpc. The SFRs of the trimmed samples at $R_\perp < 30$ kpc remain offset by ~ 0.6 dex, however, and we must consider this caveat as we proceed with our comparison of the W_{2796} distributions of these subsamples.

We now wish to compare the median and dispersion in W_{2796} in each of these trimmed samples. However, because many of our PRIMUS sightlines yield only upper limits on W_{2796}, it is not straightforward to calculate these statistics from analysis of the measurements of W_{2796} in individual spectra. Instead, we coadd our spectroscopy of these sightlines to obtain the median normalized flux value as a function of wavelength, and use a bootstrapping analysis to estimate the dispersion in these flux values. We then perform absorption line

analysis on the resulting coadds to assess the median and dispersion in W_{2796}.

In detail, we first expunge those spectra having particularly low S/N (i.e., S/N(Mg II) < 4 Å^{-1}), as we have found that the poor continuum normalization of these sightlines can introduce spurious features into the final coadds (see, e.g., the Mg II profile for object 1611 in Appendix Figure 18). In practice, this eliminates only two sightlines from the subsamples at 30 kpc $< R_\perp <$ 50 kpc and 50 kpc $< R_\perp <$ 150 kpc, and does not eliminate any sightlines within 30 kpc. Then, using the method described in Section 3 of Prochaska et al. (2014), we linearly interpolate the continuum-normalized flux in each remaining spectrum onto 100 km s^{-1}-wide pixels. We determine the median flux in each pixel to construct the final median spectrum. We also generate 100 bootstrap samples of the spectra, calculating the median of each in the same manner. Finally, we determine the continuum level of the resulting coadds via a linear fit in the velocity windows -3000 km s^{-1} $< \delta v < -385$ km s^{-1} and 1155 km s^{-1} $< \delta v <$ 3000 km s^{-1} (with $\delta v = 0$ km s^{-1} at $\lambda = 2796.35$ Å), renormalizing each coadd to ensure it has a continuum level ≈ 1. We measure the equivalent width of the Mg II λ2796 feature in the coadds in the relative velocity window -385 km s^{-1} $< \delta v <$ 385 km s^{-1}, such that the red edge of this range falls at the midpoint between the λ2796.35 and λ2803.53 transitions. The median coadds of the spectra in each of the trimmed PRIMUS subsamples described above are shown in Figure 13.

The W_{2796} measured from each of these coadds are shown in orange in Figure 14. The vertical error bars on these points indicate the $\pm 1\sigma$ dispersion in W_{2796} measured from the 100 bootstrap realizations of the median coadds described above. We measure a large median $W_{2796} = 0.95 \pm 0.29$ Å at $R_\perp < 30$ kpc. At 30 kpc $< R_\perp <$ 50 kpc, the sample absorption strength is significantly weaker, with a median $W_{2796} = 0.22 \pm 0.16$ Å. Finally, at $R_\perp > 50$ kpc, our sightlines exhibit a median W_{2796} similar to that of the 30 kpc $< R_\perp <$ 50 kpc sample, albeit with a large scatter. Indeed, the comparably large W_{2796} values at these large impact parameters likely give rise to the flat best-fit $\log W_{2796} - R_\perp$ relation discussed in §7.1. Again, we note that in QSO-galaxy pair studies targeting the CGM of relatively isolated f/g galaxies, the average/median W_{2796} has been ubiquitously observed to *decline* with increasing $R_\perp$. These differences are suggestive of a physical effect which enhances W_{2796} in the extended environments of magnitude-selected galaxies. We require a larger and higher-S/N sample at $R_\perp > 50$ kpc to confirm this overall trend.

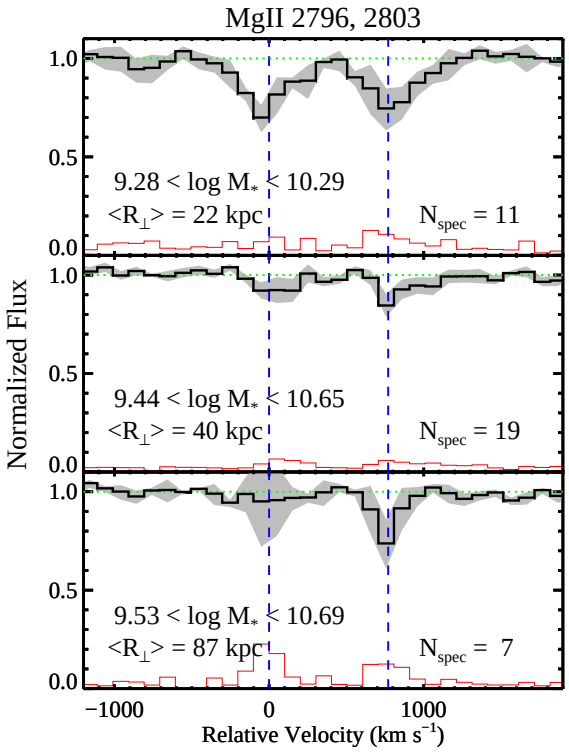

Figure 13. Coadded spectra (black) of our PRIMUS b/g galaxy sightlines in the region around the Mg II 2796, 2803 transition. The spectra in the top, middle, and bottom panels include all pairs in the orange filled histograms in the left-, middle-, and right-hand columns of Figure 12, respectively, except for those pairs with b/g spectra having S/N(Mg II) < 4 Å^{-1}. The mean $R_\perp$ of all sightlines in each coadd is noted at the lower left of each panel, and the number of sightlines is noted at lower right. The filled gray curves show the $\pm$34th-percentile interval for the fluxes in our bootstrap sample in each pixel. The red histogram shows this same 1σ error array. The vertical blue dashed lines mark the rest velocity of each transition in the Mg II doublet.

We also calculate the median and dispersion in W_{2796} in each of the QSO-galaxy comparison subsamples within $R_\perp < 50$ kpc defined in Figure 12, and show the results in cyan in Figure 14. Working with the W_{2796} measurements themselves (rather than the QSO spectra), we estimate the dispersion by using an iterative sigma-clipping algorithm to identify outliers defined to lie $> 3\sigma$ from the central value (as in our estimate of the dispersion in the bootstrap samples above). We iteratively mask these outliers, compute the central value of the distribution, and reassess the dispersion in W_{2796} taking this new central value into account. Among the 38 QSO sightlines considered here, only four do not yield significant detections of Mg II absorption, such that our estimates of the sample dispersion will not be signifi-

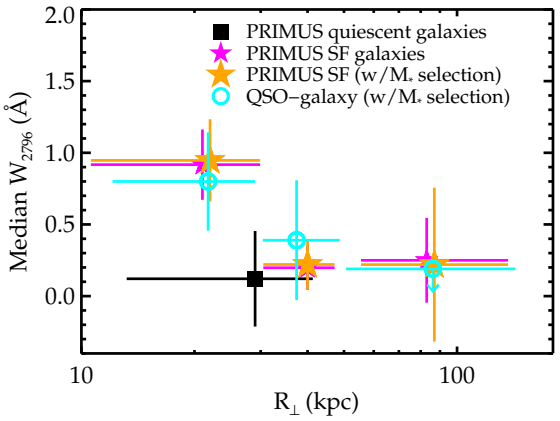

Figure 14. Median W_{2796} in coadded spectra of the subsamples of PRIMUS sightlines described in §7.3 and shown in Figure 13 (filled orange stars). The filled magenta stars show the median W_{2796} in the coadded spectra of all PRIMUS sightlines probing f/g star-forming galaxy halos and having S/N(Mg II) > 4 Å^{-1} at $R_\perp < 30$ kpc, 30 kpc $< R_\perp <$ 50 kpc, and $R_\perp > 50$ kpc (i.e., the galaxies shown with the open orange histograms in Figure 12). The filled black square shows W_{2796} measured in the coadded spectrum of PRIMUS sightlines probing quiescent f/g galaxy halos (shown in Figure 15). The vertical error bars indicate the dispersion in W_{2796} measured from median coadds of 100 bootstrap realizations of each subsample. The open cyan circles at $R_\perp < 50$ kpc show the median W_{2796} and dispersion in the W_{2796} values in the individual QSO-galaxy comparison sightlines included in each trimmed subsample described in §7.3. The open cyan circle at $R_\perp = 86$ kpc is placed at the upper 25th-percentile value of the cumulative distribution function of W_{2796} values in the QSO-galaxy comparison dataset with $R_\perp > 50$ kpc, and is calculated using the `ASURV` software package. The x-axis locations of the points are set by the mean $R_\perp$ of the sightlines in each coadd, and the horizontal error bars show the full range in these values. The subsamples represented by the orange and cyan points have been selected to cover the same ranges in M_* in each $R_\perp$ bin, and have similar median M_* values.

cantly biased by the inclusion of censored measurements. As the majority of QSO sightlines at $R_\perp > 50$ kpc yield upper limits, we again turn to the `ASURV` survival analysis software to quantify the W_{2796} distribution at these large impact parameters, placing the cyan upper limit in Figure 14 at the upper 25th-percentile of the Kaplan-Meier estimator for the distribution function of W_{2796} values. This figure demonstrates a striking similarity between the W_{2796} in the PRIMUS and QSO-galaxy comparison samples, particularly at $R_\perp < 50$ kpc. We note that the dispersion in the QSO-galaxy subsample is somewhat larger at 30 kpc $< R_\perp <$ 50 kpc, and will discuss potential reasons for this discrepancy in Paper II. Overall, we interpret these measurements as suggestive that the CGM of galaxies having a comparable range in M_* give rise to similar Mg II absorption strength toward both our b/g galaxy sightlines at $z_{\rm f/g} \sim 0.4$ and toward b/g QSO sightlines at $z_{\rm f/g} \sim 0.2$.

Finally, to assess the strength of Mg II aborption surrounding the quiescent galaxies in our sample, we coadd spectroscopy of five sightlines passing within $R_\perp < 50$ kpc of objects sitting below the threshold for star-forming systems discussed in §5 and show the resulting stack in Figure 15. The coadd does not exhibit detectable absorption, yielding a median $W_{2796} = 0.12 \pm 0.33$ Å. This measurement is consistent with the median W_{2796} measured for each of the PRIMUS star-forming f/g galaxy subsamples at $R_\perp > 30$ kpc, and is discrepant by only 1.9σ with the median W_{2796} for star-forming galaxies within $R_\perp < 30$ kpc. We also note that f/g Mg II absorption is indeed securely detected toward two of these five sightlines individually (having galaxy pair IDs 405 and 611, and $W_{2796} = 0.73 \pm 0.34$ Å and 0.73 ± 0.32 Å), suggestive of a large dispersion in absorption strength in quiescent galaxy environments. A few previous studies have presented evidence for weaker Mg II absorption around host galaxies which are redder in color: e.g., Gauthier & Chen (2011) reported a lower incidence of strong Mg II absorbers around quiescent Luminous Red Galaxies (LRGs) than around $\lesssim L^*$ galaxies at $z \sim 0.2 - 0.3$; and Bordoloi et al. (2011) measured weaker Mg II absorption in stacked spectra probing red vs. blue f/g hosts. While the central value of our W_{2796} measurement around star-forming hosts at $R_\perp < 30$ kpc is indeed higher than the same measurement around quiescent systems, we lack the S/N required to confirm the detection of this trend. We present a more detailed comparison to the results of Bordoloi et al. (2011) in the following subsection.

7.4. *Comparison with the CGM Probed by Stacked Background Sightline Samples*

As a final test of the consistency of our measurements with the literature, here we compare our results to those of additional studies which have constrained halo Mg II absorption properties via the coaddition of numerous low-S/N spectra of background sightlines. The primary comparison study, Bordoloi et al. (2011), mined the zCOSMOS galaxy redshift survey (Lilly et al. 2007) for projected galaxy pairs within $R_\perp < 200$ kpc. The ~ 4000 f/g galaxies satisfying their selection criteria span a redshift range $0.5 < z < 0.9$. The zCOSMOS spectra of the b/g galaxies have a low spectral resolution ($R \sim 200$) and hence cannot resolve the two transitions

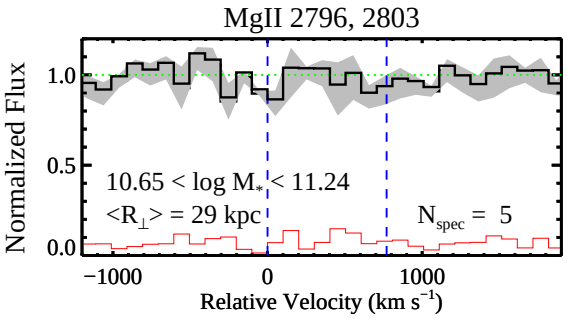

Figure 15. Coadded spectra (black) of our PRIMUS b/g galaxy sightlines probing quiescent f/g galaxy halos in the region around the Mg II 2796, 2803 transition. All spectra probe within $R_\perp < 50$ kpc and have S/N(Mg II) > 4 Å^{-1}. The filled gray curves show the ±34th-percentile interval for the fluxes in our bootstrap sample in each pixel. The red histogram shows this same 1σ error array. Plot labels and horizontal and vertical dashed lines are as described in the caption of Figure 13.

in the Mg II doublet. Therefore, this work reported the median equivalent width of the blended doublet ($W_{\rm MgII}$) detected in coadded spectra of subsamples of $\sim 75-150$ b/g spectra.

Bordoloi et al. (2011) investigated the dependence of $W_{\rm MgII}$ on several f/g host galaxy properties, including color, stellar mass, environment, and orientation. Given the galaxy characteristics already at hand for the PRIMUS sample, we choose to compare to the Bordoloi et al. (2011) subsamples selected by a combination of stellar mass and color. To differentiate between blue and red galaxies, these authors invoked a division in $(u-B)$ color just slightly bluer than that inspired by Peng et al. (2010):

$$(u-B)_{\rm AB} = 0.98 + 0.075 \log \frac{M_*}{10^{10}\ M_\odot} - 0.18z. \quad (4)$$

We note that the locus of this cut sits blueward of the minimum of the bimodal galaxy distribution, such that some star-forming galaxies fall into the "red" subsample.

Though the passbands used to calculate this color are not explicitly specified, we assume that the quantity $(u-B)$ is similar to the $(U-B)$ color we use in Figure 4a and apply this cut without adjustment to our f/g galaxy sample. Bordoloi et al. (2011) further subdivided these blue and red samples by stellar mass, separating the blue galaxies into bins above and below $\log M_*/M_\odot = 9.88$ and the red galaxies at $\log M_*/M_\odot = 10.68$. We adopt the same subdivisions for the portion of our pair sample having $R_\perp < 50$ kpc, finding that the resulting blue galaxy subsamples each contain > 10 sightlines, while the red galaxy subsamples contain just handfuls of objects (4-6). We show the coadded spectra for these four subsamples in Figure 16, with the top two panels showing the coadds of the low- and high-M_* blue subsamples, and the bottom panels showing the coadds of our red subsamples. Strong absorption is evident in the blue, high-M_* panel, while the blue, low-M_* and red subsamples each exhibit a weak absorption signal.

To determine the total absorption from both doublet transitions (for consistency with Bordoloi et al.), we measure the equivalent width in these spectra over a velocity window -385 km s$^{-1} < \delta v < 1155$ km s^{-1}, which spans an interval from 385 km s^{-1} blueward of the λ2796 transition to 385 km s^{-1} redward of the λ2803 transition. The resulting median $W_{\rm MgII}$ values are plotted with filled stars in Figure 17, along with the analogous measurements from Bordoloi et al. (2011, shown with open triangles)[8]. The filled red circle shows a measurement of the mean $W_{\rm MgII}$ within $R_\perp < 45$ kpc of a sample of 35 $z \sim 0.5$ LRGs assessed using coadded SDSS QSO spectra by Zhu et al. (2014). The x-axis value of this point is the median stellar mass of the full sample of LRGs used in this study ($\log M_*/M_\odot = 11.4$), which includes galaxies in projected LRG-QSO pairs with separations as large as $R_\perp = 18$ Mpc.

The large dispersion in the $W_{\rm MgII}$ values measured from the PRIMUS subsamples (and their small sizes) again limits our ability to draw firm conclusions from this analysis. However, we note the close consistency between the $W_{\rm MgII}$ measured around the low-M_* blue galaxy subsamples drawn from both PRIMUS and Bordoloi et al. (2011). The $W_{\rm MgII}$ measurements for the remaining PRIMUS subsamples tend to have higher central values than those from zCOSMOS, with the high-M_* blue subsamples having an offset of the greatest significance (1.7σ). And while the median $W_{\rm MgII}$ values for the red PRIMUS samples are indeed lower than that measured for the high-M_* blue subsample, overall we fail to reproduce the highly significant offset between $W_{\rm MgII}$ around blue vs. red galaxies reported in the zCOSMOS analysis. The results shown in Figure 14 are similarly suggestive of lower W_{2796} around quiescent vs. star-forming galaxies, but again, these measurements are discrepant at $\lesssim 2\sigma$. Given that the Bordoloi et al. (2011) subsamples all include at least 99 pairs, this discrepancy may arise simply due to stochasticity in our sparse sampling of the red galaxy population. However,

[8] Bordoloi et al. (2011) estimated uncertainty in $W_{\rm MgII}$ using a bootstrapping approach, generating 1000 coadds from sets of random draws from each subsample. The dispersion in $W_{\rm MgII}$ among this sample of 1000 was adopted as the error in this quantity.

we also note that the trend of lower $W_{\rm MgII}$ around redder host galaxies is not reproduced in higher-S/N studies of individual projected QSO-galaxy pairs. For instance, Nielsen et al. (2013) found no significant difference in the incidence of Mg II absorbers around blue vs. red galaxies within $R_\perp < 50$ kpc, even after testing several limiting W_{2796} values (of 0.1, 0.3, 0.6, and 1.0 Å). Chen et al. (2010a) likewise reported no strong dependence of W_{2796} on f/g galaxy color. This apparent disagreement in the literature may be resolved with larger samples of sightlines (surpassing those of Bordoloi et al. in size) probing each of these galaxy subpopulations.

8. SUMMARY

We have presented spectroscopy of 72 projected pairs of galaxies selected from the PRIsm MUlti-object Survey redshift catalog (Coil et al. 2011b) with impact parameters $R_\perp < 150$ kpc. Fifty-one of these pairs have $R_\perp < 50$ kpc, and hence probe circumgalactic environments known to yield strong intervening absorption traced by the Mg II transition. The sample foreground (f/g) galaxies span a range in redshifts $0.35 < z_{\rm f/g} < 0.8$ and include both star-forming and quiescent systems to a stellar mass limit $M_* \gtrsim 10^9\ M_\odot$. The background (b/g) galaxies, selected to a magnitude limit $B_{\rm AB} \lesssim 22.3$, are distributed in redshift over the range $0.4 < z_{\rm b/g} < 2.0$. While a third of these galaxies host bright AGN which give rise to broad emission line features, the remaining b/g sightlines exhibit no signs of broad-line AGN in their optical spectroscopy. The ~ 20 of these latter systems which have been imaged by *HST*/ACS have half-light radii in the range 2 kpc $\lesssim R_{\rm eff} \lesssim 8$ kpc estimated at the redshift of the corresponding f/g system.

Our spectroscopy covers the Mg II $\lambda\lambda 2796, 2803$ doublet in the rest-frame of the foreground galaxy at high S/N, constraining the Mg II equivalent width to a typical limit $W_{2796} \gtrsim 0.5$ Å in individual b/g galaxy sightlines. We make secure ($> 2\sigma$ significant) detections of the $\lambda 2796$ transition in 20 sightlines passing within $R_\perp < 50$ kpc, and place a 2σ upper limit on W_{2796} of < 0.5 Å in an additional 11 close sightlines. This is the first work presenting a sample of more than $\sim 1-2$ individual b/g galaxy sightlines with securely-detected absorbers arising from intervening systems.

We have shown that the W_{2796} associated with the f/g galaxy halos in this sample declines with increasing $R_\perp$ of the b/g galaxy within $R_\perp < 50$ kpc, consistent with the findings of numerous works probing the circumgalactic medium (CGM) of f/g galaxies with similar properties using b/g QSO sightlines. Our analysis additionally constrains the intrinsic scatter in the relationship between $R_\perp$ and W_{2796} (§7.1). We have demonstrated

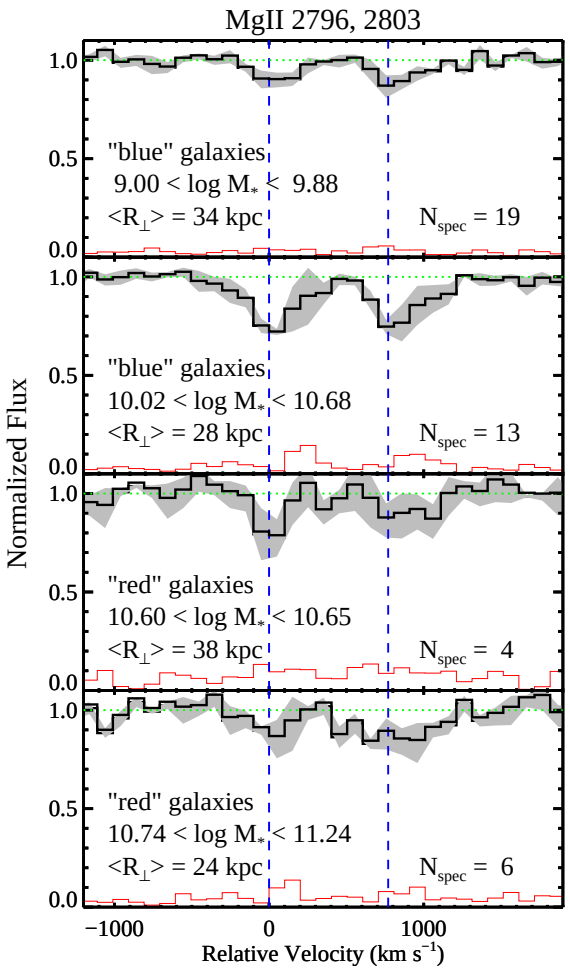

Figure 16. Coadded spectra (black) of PRIMUS b/g galaxy sightlines probing blue, low-M_* galaxies (top), blue, high-M_* galaxies (top middle), red, low-M_* galaxies (bottom middle), and red, high-M_* galaxies (bottom) in the region around the Mg II 2796, 2803 transitions. The specific color and M_* selection criteria used are described in §7.4 (see Eq. 7.4) and are chosen to match the sample selection of Bordoloi et al. (2011). All spectra probe within $R_\perp < 50$ kpc and have S/N(Mg II) > 4 Å^{-1}. The filled gray curves show the ±34th-percentile interval for the fluxes in our bootstrap sample in each pixel. The red histogram shows this same 1σ error array. Plot labels and horizontal and vertical dashed lines are as described in the caption of Figure 13.

that W_{2796} is higher around galaxies with higher SFR and/or stellar mass, and have shown that these trends are exhibited with statistical significance within the "inner" CGM (at 30 kpc $< R_\perp < 50$ kpc in the case of M_* and at $R_\perp < 30$ kpc in the case of SFR; §7.2). Qualitatively similar trends are likewise exhibited in projected QSO-galaxy pair studies of circumgalactic Mg II absorp-

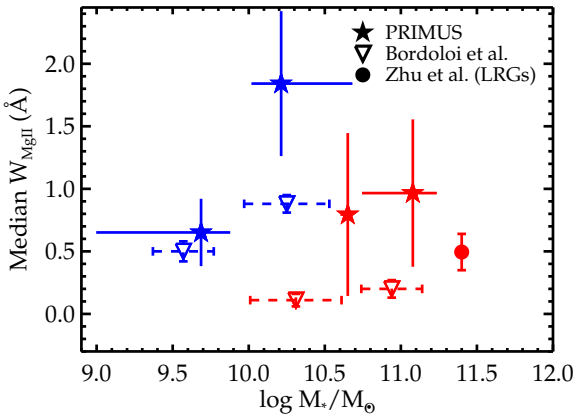

Figure 17. Median $W_{\rm MgII}$ in coadded spectra of subsamples of PRIMUS sightlines described in §7.4 and shown in Figure 16. The filled red stars show the median $W_{\rm MgII}$ in the red PRIMUS subsamples, while the filled blue stars show the same measurement for the blue PRIMUS subsamples. The x-axis locations are set by the median $\log M_*/M_\odot$ value for the subsamples, and the error bars in the x-direction show the full range in these values. The error bars in the y-direction indicate the dispersion in $W_{\rm MgII}$ measured from median coadds of 100 bootstrap realizations of each subsample. The open triangles show measurements of median $W_{\rm MgII}$ around subsamples of blue and red galaxies from Bordoloi et al. (2011). The x-axis values and uncertainty intervals of these points indicate the mean and $\pm1\sigma$ dispersion in $\log M_*/M_\odot$ values in each subsample. The filled circle shows the mean $W_{\rm MgII}$ measured in coadded QSO sightlines passing within 45 kpc of $z\sim0.5$ LRGs reported in Zhu et al. (2014).

tion at $z<1$. Finally, we have shown that the median W_{2796} observed toward both b/g galaxies and a sample of b/g QSOs taken from the literature which probe the environments of f/g galaxies with a similar range in M_* at similar impact parameters are statistically consistent (§7.3).

All together, these findings point to a broad-brush conformity in the mean properties of the CGM as observed toward both extended (> kpc) galaxy b/g beams and the pencil-beam ($<10^{-2}$ pc) sightlines offered by b/g QSOs. In Paper II, we will compare this sample of Mg II absorbers and those observed toward b/g QSOs in more detail, focusing in particular on the dispersion in their respective equivalent width distributions. With the adoption of a few simplifying assumptions, we will demonstrate that together, these two datasets set a lower limit on the coherence scale of Mg II-absorbing circumgalactic material. Such a limit is unique in the context of CGM studies, and has important implications for the mass, survival time, and origin of the cool, photoionized gas which pervades galaxy environments.

K.H.R.R acknowledges support for this project from the Clay Postdoctoral Fellowship, and from the Alexander von Humboldt foundation in the form of the Humboldt Postdoctoral Fellowship. The Humboldt foundation is funded by the German Federal Ministry for Education and Research. A.L.C. acknowledges support from NSF CAREER award AST-1055081. Funding for PRIMUS is provided by NSF (AST-0607701, AST-0908246, AST-0908442, AST-0908354) and NASA (Spitzer-1356708, 08-ADP08-0019, NNX09AC95G).

These findings are in part based on observations collected at the European Organisation for Astronomical Research in the Southern Hemisphere under ESO programs 088.A-0529(A) and 090.A-0485(A). In addition, a significant portion of the data presented herein were obtained at the W. M. Keck Observatory, which is operated as a scientific partnership among the California Institute of Technology, the University of California, and the National Aeronautics and Space Administration. The Observatory was made possible by the generous financial support of the W. M. Keck Foundation.

The authors wish to thank the CFHTLS, COSMOS, and SWIRE teams for making their data and catalogs public. We acknowledge Robert da Silva for his guidance in the use of the SLUG software package. We thank James Bullock, Joe Hennawi, and Brice Ménard for insightful comments on this analysis, and we gratefully acknowledge Xavier Prochaska for sharing code to generate spectroscopic coadds, and for numerous valuable discussions of this work and his reading of an earlier version of this manuscript.

Finally, the authors wish to recognize and acknowledge the very significant cultural role and reverence that the summit of Mauna Kea has always had within the indigenous Hawaiian community. We are most fortunate to have the opportunity to conduct observations from this mountain.

REFERENCES

Adelberger, K. L., Shapley, A. E., Steidel, C. C., et al. 2005, ApJ, 629, 636

Appenzeller, I., Fricke, K., Fürtig, W., et al. 1998, The Messenger, 94, 1

Barger, A. J., Cowie, L. L., & Wang, W.-H. 2008, ApJ, 689, 687
Bergeron, J., & Stasińska, G. 1986, A&A, 169, 1
Berti, A. M., Coil, A. L., Behroozi, P. S., et al. 2016, ArXiv e-prints, arXiv:1608.05084
Bertin, E., & Arnouts, S. 1996, A&AS, 117, 393
Bigelow, B. C., & Dressler, A. M. 2003, in Society of Photo-Optical Instrumentation Engineers (SPIE) Conference Series, Vol. 4841, Instrument Design and Performance for Optical/Infrared Ground-based Telescopes, ed. M. Iye & A. F. M. Moorwood, 1727–1738
Binney, J., Nipoti, C., & Fraternali, F. 2009, MNRAS, accepted (arXiv:0902.4525), arXiv:0902.4525
Bond, N. A., Churchill, C. W., Charlton, J. C., & Vogt, S. S. 2001, ApJ, 562, 641
Bordoloi, R., Lilly, S. J., Knobel, C., et al. 2011, ApJ, 743, 10
Bordoloi, R., Tumlinson, J., Werk, J. K., et al. 2014, ApJ, 796, 136
Bouché, N., Hohensee, W., Vargas, R., et al. 2012, MNRAS, 3207
Bouché, N., Murphy, M. T., Kacprzak, G. G., et al. 2013, Science, 341, 50
Burchett, J. N., Tripp, T. M., Prochaska, J. X., et al. 2015, ApJ, 815, 91
Chabrier, G. 2003, PASP, 115, 763
Chabrier, G. 2005, in Astrophysics and Space Science Library, Vol. 327, The Initial Mass Function 50 Years Later, ed. E. Corbelli, F. Palla, & H. Zinnecker, 41
Chen, H., Helsby, J. E., Gauthier, J., et al. 2010a, ApJ, 714, 1521
Chen, H.-W., Lanzetta, K. M., & Webb, J. K. 2001, ApJ, 556, 158
Chen, H.-W., Wild, V., Tinker, J. L., et al. 2010b, ApJL, 724, L176
Churchill, C. W., Mellon, R. R., Charlton, J. C., et al. 2000, ApJS, 130, 91
Churchill, C. W., Trujillo-Gomez, S., Nielsen, N. M., & Kacprzak, G. G. 2013, ApJ, 779, 87
Cohen, J. G., Cromer, J., & Southard, Jr., S. 1994, in Astronomical Society of the Pacific Conference Series, Vol. 61, Astronomical Data Analysis Software and Systems III, ed. D. R. Crabtree, R. J. Hanisch, & J. Barnes, 469–+
Coil, A. L., Weiner, B. J., Holz, D. E., et al. 2011a, ApJ, 743, 46
Coil, A. L., Blanton, M. R., Burles, S. M., et al. 2011b, ApJ, 741, 8
Conroy, C., & Gunn, J. E. 2010, ApJ, 712, 833
Cooke, J., & O'Meara, J. M. 2015, ApJL, 812, L27
Cool, R. J., Moustakas, J., Blanton, M. R., et al. 2013, ApJ, 767, 118
Crighton, N. H. M., Hennawi, J. F., & Prochaska, J. X. 2013, ApJL, 776, L18
Crighton, N. H. M., Hennawi, J. F., Simcoe, R. A., et al. 2014, ArXiv e-prints, arXiv:1406.4239
da Silva, R. L., Fumagalli, M., & Krumholz, M. 2012, ApJ, 745, 145
Danforth, C. W., & Shull, J. M. 2008, ApJ, 679, 194
Davis, M., Faber, S. M., Newman, J., et al. 2003, in Society of Photo-Optical Instrumentation Engineers (SPIE) Conference Series, Vol. 4834, Society of Photo-Optical Instrumentation Engineers (SPIE) Conference Series, ed. P. Guhathakurta, 161–172
Diamond-Stanic, A. M., Coil, A. L., Moustakas, J., et al. 2015, ArXiv e-prints, arXiv:1507.01945
Fall, S. M., Chandar, R., & Whitmore, B. C. 2009, ApJ, 704, 453
Farina, E. P., Falomo, R., Scarpa, R., et al. 2014, MNRAS, 441, 886
Feigelson, E. D., & Nelson, P. I. 1985, ApJ, 293, 192
Foreman-Mackey, D., Hogg, D. W., Lang, D., & Goodman, J. 2013, PASP, 125, 306
Frank, S., Bentz, M. C., Stanek, K. Z., et al. 2007, Ap&SS, 312, 325
Gauthier, J.-R., & Chen, H.-W. 2011, MNRAS, 418, 2730
Giacconi, R., Rosati, P., Tozzi, P., et al. 2001, ApJ, 551, 624
Giavalisco, M., Ferguson, H. C., Koekemoer, A. M., et al. 2004, ApJL, 600, L93
Grasha, K., Calzetti, D., Adamo, A., et al. 2015, ApJ, 815, 93
Ilbert, O., Capak, P., Salvato, M., et al. 2009, ApJ, 690, 1236
Johnson, S. D., Chen, H.-W., & Mulchaey, J. S. 2015, MNRAS, 452, 2553
Kacprzak, G. G., Churchill, C. W., & Nielsen, N. M. 2012, ArXiv e-prints, arXiv:1205.0245
Kacprzak, G. G., Churchill, C. W., Steidel, C. C., & Murphy, M. T. 2008, AJ, 135, 922
Kereš, D., Katz, N., Weinberg, D. H., & Davé, R. 2005, MNRAS, 363, 2
Krumholz, M. R., Fumagalli, M., da Silva, R. L., Rendahl, T., & Parra, J. 2015a, MNRAS, 452, 1447
Krumholz, M. R., Adamo, A., Fumagalli, M., et al. 2015b, ApJ, 812, 147
Lada, C. J., & Lada, E. A. 2003, ARA&A, 41, 57
Lan, T.-W., Ménard, B., & Zhu, G. 2014, ApJ, 795, 31
Lanzetta, K. M., & Bowen, D. 1990, ApJ, 357, 321

Lavalley, M., Isobe, T., & Feigelson, E. 1992, in Astronomical Society of the Pacific Conference Series, Vol. 25, Astronomical Data Analysis Software and Systems I, ed. D. M. Worrall, C. Biemesderfer, & J. Barnes, 245

Leauthaud, A., Massey, R., Kneib, J.-P., et al. 2007, ApJS, 172, 219

Lee, K.-G., Hennawi, J. F., Stark, C., et al. 2014, ApJL, 795, L12

Lee, K.-G., Hennawi, J. F., White, M., et al. 2016, ApJ, 817, 160

Lehner, N., Savage, B. D., Richter, P., et al. 2007, ApJ, 658, 680

Lehner, N., Howk, J. C., Tripp, T. M., et al. 2013, ApJ, 770, 138

Lilly, S. J., Le Fèvre, O., Renzini, A., et al. 2007, ApJS, 172, 70

Maller, A. H., & Bullock, J. S. 2004, MNRAS, 355, 694

Martin, C. L., Shapley, A. E., Coil, A. L., et al. 2012, ArXiv e-prints, arXiv:1206.5552

McCourt, M., O'Leary, R. M., Madigan, A.-M., & Quataert, E. 2015, MNRAS, 449, 2

Mendez, A. J., Coil, A. L., Aird, J., et al. 2016, ApJ, 821, 55

Moustakas, J., Coil, A. L., Aird, J., et al. 2013, ApJ, 767, 50

Murray, N., Quataert, E., & Thompson, T. A. 2010, ApJ, 709, 191

Nielsen, N. M., Churchill, C. W., & Kacprzak, G. G. 2013, ApJ, 776, 115

Nielsen, N. M., Churchill, C. W., Kacprzak, G. G., Murphy, M. T., & Evans, J. L. 2015, ApJ, 812, 83

Oliver, S., Rowan-Robinson, M., Alexander, D. M., et al. 2000, MNRAS, 316, 749

Peng, Y.-j., Lilly, S. J., Kovač, K., et al. 2010, ApJ, 721, 193

Pierre, M., Valtchanov, I., Altieri, B., et al. 2004, JCAP, 9, 11

Prochaska, J. X., Hennawi, J. F., & Simcoe, R. A. 2013a, ApJL, 762, L19

Prochaska, J. X., Kasen, D., & Rubin, K. 2011, ArXiv e-prints, arXiv:1102.3444

Prochaska, J. X., Wingyee Lau, M., & Hennawi, J. F. 2014, ArXiv e-prints, arXiv:1409.6344

Prochaska, J. X., Hennawi, J. F., Lee, K.-G., et al. 2013b, ApJ, 776, 136

Rees, M. J., & Ostriker, J. P. 1977, MNRAS, 179, 541

Rubin, K. H. R., Hennawi, J. F., Prochaska, J. X., et al. 2015, ApJ, 808, 38

Rubin, K. H. R., Prochaska, J. X., Koo, D. C., et al. 2014, ApJ, 794, 156

Rubin, K. H. R., Prochaska, J. X., Koo, D. C., Phillips, A. C., & Weiner, B. J. 2010a, ApJ, 712, 574

Rubin, K. H. R., Weiner, B. J., Koo, D. C., et al. 2010b, ApJ, 719, 1503

Schaye, J., Carswell, R. F., & Kim, T.-S. 2007, MNRAS, 379, 1169

Scoville, N., Abraham, R. G., Aussel, H., et al. 2007, ApJS, 172, 38

Shakura, N. I., & Sunyaev, R. A. 1973, A&A, 24, 337

Simcoe, R. A., Sargent, W. L. W., & Rauch, M. 2004, ApJ, 606, 92

Speagle, J. S., Steinhardt, C. L., Capak, P. L., & Silverman, J. D. 2014, ApJS, 214, 15

Steidel, C. C. 1995, in QSO Absorption Lines, ed. G. Meylan, 139–+

Steidel, C. C., Erb, D. K., Shapley, A. E., et al. 2010, ApJ, 717, 289

Tripp, T. M., Meiring, J. D., Prochaska, J. X., et al. 2011, Science, 334, 952

Weiner, B. J., Coil, A. L., Prochaska, J. X., et al. 2009, ApJ, 692, 187

Werk, J. K., Prochaska, J. X., Thom, C., et al. 2013, ApJS, 204, 17

Werk, J. K., Prochaska, J. X., Tumlinson, J., et al. 2014, ArXiv e-prints, arXiv:1403.0947

Willmer, C. N. A., Faber, S. M., Koo, D. C., et al. 2006, ApJ, 647, 853

Wirth, G. D., Willmer, C. N. A., Amico, P., et al. 2004, AJ, 127, 3121

Wittman, D. M., Tyson, J. A., Dell'Antonio, I. P., et al. 2002, in Society of Photo-Optical Instrumentation Engineers (SPIE) Conference Series, Vol. 4836, Survey and Other Telescope Technologies and Discoveries, ed. J. A. Tyson & S. Wolff, 73–82

Zhu, G., Ménard, B., Bizyaev, D., et al. 2014, MNRAS, 439, 3139

Table 1. Galaxy Pair Targets

Pair ID	Background Galaxy		Foreground Galaxy		$z_{b/g}^{PR\,a}$	$z_{f/g}^{PR\,a}$	$z_{b/g}{}^{b}$	$z_{f/g}{}^{b}$	B_{AB}(b/g)	B_{AB}(f/g)	Angular Separation
	R.A.	Decl.	R.A.	Decl.							arcsec
101	23:26:33.73	+00:00:04.1	23:26:33.89	-00:00:03.0	0.85	0.49	0.84640	0.49274	21.9	21.9	7.52
102	23:27:29.20	+00:20:27.6	23:27:29.04	+00:20:29.7	1.35	1.24	1.34876	1.24400	22.2	23.6	3.19
103*	23:30:55.20	+00:05:57.5	23:30:54.90	+00:05:54.9	0.69	0.48	0.69275	0.47989	21.4	22.7	5.12
104*	23:30:50.56	+00:15:55.8	23:30:50.63	+00:16:02.0	1.94	0.41	1.94227	0.40986	19.9	23.1	6.35
201	02:16:17.89	-04:32:04.6	02:16:17.42	-04:32:01.8	0.50	0.44	0.49836	0.44695	22.0	22.7	7.51
202	02:16:15.62	-04:32:59.8	02:16:15.79	-04:33:02.1	0.67	0.53	0.66387	0.66415	21.7	22.7	3.49
203	02:15:33.15	-04:26:11.5	02:15:32.80	-04:26:08.7	0.50	0.35	0.50979	0.35138	22.0	21.5	5.92
204	02:17:50.82	-04:16:00.3	02:17:50.70	-04:15:57.0	0.61	0.45	0.60910	0.44265	21.8	22.2	3.74
207*	02:21:08.80	-03:59:44.0	02:21:08.38	-03:59:40.0	0.68	0.43	0.68732	0.43092	21.5	22.7	7.48
208*	02:20:49.50	-04:30:31.2	02:20:49.54	-04:30:28.7	1.81	0.60	1.81307	0.59729	22.0	22.2	2.57
209	02:22:12.28	-05:07:24.0	02:22:12.14	-05:07:24.8	0.62	0.35	0.61682	0.35012	21.7	22.5	2.23
210	02:21:09.56	-04:55:25.5	02:21:09.64	-04:55:26.2	0.88	0.79	0.87675	0.80620	22.3	22.9	1.41
211	02:22:24.78	-05:02:29.0	02:22:25.05	-05:02:31.3	0.58	0.41	0.57994	0.40878	21.7	21.5	4.68
212*	02:20:05.32	-05:19:14.9	02:20:05.51	-05:19:21.3	1.91	0.55	1.91296	0.55047	21.0	23.3	6.97
213	02:20:41.35	-05:35:30.2	02:20:41.33	-05:35:32.7	0.62	0.47	0.61605	0.46911	21.6	22.3	2.57
216*	02:23:07.94	-04:59:09.0	02:23:07.79	-04:59:09.2	1.33	0.36	1.32355	—	20.5	23.1	2.31
217	02:23:20.72	-05:32:08.7	02:23:20.27	-05:32:08.8	0.49	0.36	0.49148	0.35417	21.1	21.2	6.86
219	02:23:10.22	-05:21:28.8	02:23:10.46	-05:21:33.1	0.44	0.36	0.43907	0.36881	21.4	22.1	5.62
221*	02:19:38.75	-05:11:03.4	02:19:38.62	-05:11:00.0	1.74	0.74	1.75261	star	21.8	23.1	3.92
223*	02:17:03.70	-04:37:38.3	02:17:04.03	-04:37:41.7	1.34	0.70	1.35232	0.74561	21.7	23.3	6.01
301*	02:28:42.03	+00:45:36.4	02:28:41.56	+00:45:40.6	1.67	0.36	1.67360	0.36276	20.3	21.6	8.24
302	02:32:17.94	+00:50:02.0	02:32:17.92	+00:50:05.9	0.46	0.35	0.47785	0.35051	21.5	22.3	3.93
402*	03:31:07.94	-28:33:58.7	03:31:07.62	-28:33:55.4	0.68	0.56	0.68496	0.56820	21.7	23.0	5.43
403*	03:31:07.94	-28:33:58.7	03:31:08.10	-28:34:05.3	0.68	0.58	0.68496	0.57017	21.7	23.4	6.85
404*	03:32:14.41	-29:17:05.8	03:32:14.37	-29:17:11.7	0.64	0.43	0.63664	0.43280	21.4	23.3	5.93
405	03:31:56.65	-29:13:14.3	03:31:57.04	-29:13:19.7	0.69	0.38	0.69596	0.38218	21.9	22.8	7.49
408	03:35:24.53	-28:56:33.6	03:35:24.48	-28:56:31.2	0.78	0.59	0.78855	0.59745	22.1	22.9	2.48
409	03:37:04.75	-28:49:14.8	03:37:04.60	-28:49:23.8	0.58	0.36	0.58391	0.35703	21.7	21.5	9.22
410	03:36:24.72	-28:42:26.2	03:36:24.36	-28:42:30.9	0.84	0.52	0.86234	0.51464	22.0	22.5	6.71
411	03:36:37.56	-28:43:02.6	03:36:38.13	-28:43:02.4	0.41	0.36	0.41642	0.36680	20.8	21.9	7.52
412	03:35:28.25	-28:47:22.4	03:35:28.02	-28:47:24.5	0.78	0.70	0.78699	0.73092	22.1	22.4	3.65
413	03:35:42.97	-28:21:36.6	03:35:42.64	-28:21:42.6	0.57	0.43	0.56530	0.42752	21.6	22.6	7.39
414	03:36:27.84	-28:26:14.5	03:36:28.29	-28:26:10.6	0.58	0.44	0.58390	0.43821	21.9	22.4	7.19
417	03:28:06.08	-28:30:57.7	03:28:06.22	-28:31:01.6	0.77	0.57	0.78619	0.56884	22.1	23.1	4.30
601	10:01:07.45	+02:26:26.1	10:01:07.11	+02:26:20.9	1.00	0.49	0.98752	0.49290	21.9	23.3	7.32
602*	10:01:18.58	+02:27:39.3	10:01:18.22	+02:27:42.8	1.05	0.53	1.04212	0.51684	21.0	23.0	6.51
603	10:01:30.53	+02:19:00.2	10:01:30.50	+02:19:03.0	0.96	0.69	0.98001	0.69700	22.3	22.8	2.81
604	09:59:31.46	+02:19:03.2	09:59:31.27	+02:19:05.0	0.72	0.66	0.73213	0.25032	22.1	22.8	3.36
605*	09:59:05.12	+02:15:30.0	09:59:04.89	+02:15:25.7	2.23	1.11	2.20732	—	21.4	22.9	5.60
606	09:59:59.81	+02:28:27.9	09:59:59.94	+02:28:35.8	0.50	0.35	0.48726	0.34656	20.9	22.8	8.14
607	09:59:45.19	+02:29:40.6	09:59:45.35	+02:29:39.5	0.55	0.49	0.54752	0.54760	21.7	23.2	2.66
608	10:00:08.41	+02:41:55.2	10:00:08.30	+02:41:56.9	0.66	0.50	0.64716	0.50361	22.0	22.0	2.38
609*	10:00:38.15	+02:49:30.5	10:00:38.45	+02:49:30.6	1.87	0.43	1.85705	0.43755	21.6	22.4	4.47
610	10:00:40.37	+02:49:02.0	10:00:40.64	+02:48:55.9	0.52	0.49	0.49556	0.49550	22.1	22.4	7.28
611	10:02:55.24	+02:32:55.4	10:02:55.06	+02:32:55.1	0.47	0.35	0.47130	0.35155	21.9	21.9	2.66
612*	10:01:20.26	+02:33:41.4	10:01:20.24	+02:33:43.8	1.83	0.39	1.84181	0.36079	20.4	22.5	2.42

Table 1 continued

Table 1 *(continued)*

Pair ID	Background Galaxy		Foreground Galaxy		$z_{b/g}^{PR\,a}$	$z_{f/g}^{PR\,a}$	$z_{b/g}{}^{b}$	$z_{f/g}{}^{b}$	B_{AB}(b/g)	B_{AB}(f/g)	Angular Separation
	R.A.	Decl.	R.A.	Decl.							arcsec
613*	10:01:24.86	+02:20:31.8	10:01:24.66	+02:20:29.7	1.71	0.72	1.71462	0.74056	21.1	22.9	3.59
614	10:02:56.98	+02:17:28.4	10:02:56.71	+02:17:30.5	0.59	0.36	0.60588	0.36360	21.7	21.1	4.50
615*	10:01:47.90	+02:14:47.2	10:01:47.72	+02:14:48.3	0.89	0.84	0.87988	0.87795	20.5	23.5	2.86
617*	09:59:00.21	+02:28:11.7	09:59:00.58	+02:28:14.9	0.66	0.49	0.65789	0.48812	21.7	22.2	6.28
619	09:59:52.87	+01:55:31.7	09:59:53.25	+01:55:33.7	0.45	0.35	0.44598	0.35244	20.9	23.2	6.03
620	10:00:22.44	+01:56:57.2	10:00:22.33	+01:56:55.2	0.72	0.44	star	0.43649	21.8	22.5	2.56
621	09:59:51.78	+02:19:37.7	09:59:52.41	+02:19:38.0	0.38	0.36	0.37802	0.35741	21.6	21.5	9.42
622	09:59:25.07	+02:38:40.9	09:59:24.95	+02:38:42.3	0.96	0.86	0.94283	0.94349	22.2	23.4	2.20
623*	10:01:47.04	+02:02:36.6	10:01:47.16	+02:02:31.2	1.18	0.84	1.17012	0.82579	21.8	23.5	5.71
624	10:01:19.79	+02:14:32.3	10:01:20.08	+02:14:32.5	0.45	0.36	0.44751	0.36054	21.7	21.7	4.27
625*	10:01:23.01	+02:08:51.2	10:01:23.21	+02:08:46.5	1.27	0.61	1.25811	0.60352	21.0	23.4	5.54
626	10:01:56.74	+02:04:58.9	10:01:56.38	+02:04:57.1	0.70	0.43	0.70399	0.42486	22.0	22.6	5.57
1100	23:30:53.46	+00:07:18.2	23:30:53.55	+00:07:30.2	0.54	0.48	—	0.48242	21.8	22.9	12.08
1101	23:31:06.44	+00:05:43.7	23:31:07.59	+00:05:25.3	0.47	0.40	0.46690	0.40722	22.0	22.0	25.16
1200*	02:18:34.40	-04:00:12.1	02:18:34.72	-04:00:06.7	1.50	0.95	1.50475	—	20.4	23.3	7.16
1201*	02:16:14.93	-04:06:26.4	02:16:15.44	-04:06:31.5	1.15	0.56	1.14869	0.56532	21.2	23.2	9.23
1202	02:20:04.83	-05:14:27.6	02:20:04.28	-05:14:49.8	0.53	0.40	0.53765	0.40820	21.0	23.2	23.68
1203	02:17:17.56	-04:42:03.1	02:17:18.63	-04:42:00.9	0.43	0.38	0.43191	0.37316	22.0	23.2	16.15
1204	02:19:45.93	-05:10:24.0	02:19:44.52	-05:10:28.8	0.93	0.39	star	0.50097	21.2	23.2	21.69
1205	02:17:10.20	-04:36:43.0	02:17:10.08	-04:36:55.6	0.59	0.37	0.60304	0.37238	21.2	22.2	12.69
1206	02:16:58.45	-04:38:47.5	02:16:56.90	-04:38:52.9	0.45	0.37	0.07124	—	21.5	23.0	23.89
1207	02:15:59.08	-04:30:46.0	02:15:58.34	-04:30:31.8	1.16	0.73	1.27964	0.74230	21.5	23.4	17.92
1208*	02:19:34.70	-04:41:41.0	02:19:35.19	-04:41:41.8	2.12	0.89	2.09599	0.83566	20.8	22.8	7.42
1209	02:17:40.60	-04:12:31.3	02:17:40.04	-04:12:47.6	0.43	0.37	0.43466	0.37102	22.0	21.6	18.35
1210*	02:18:09.32	-04:27:56.9	02:18:09.40	-04:28:05.1	1.55	0.58	1.53694	0.59573	21.6	23.0	8.32
1300	02:32:11.66	+00:43:34.4	02:32:10.94	+00:43:23.3	0.82	0.54	0.81118	0.58506	21.3	23.2	15.42
1400*	03:35:01.74	-28:53:47.5	03:35:02.40	-28:53:33.5	2.02	0.37	2.03408	—	19.8	22.6	16.46
1401	03:36:59.69	-28:55:12.1	03:37:00.04	-28:54:57.5	0.67	0.46	star	0.46915	19.9	22.7	15.33
1402	03:36:21.62	-28:29:59.7	03:36:20.96	-28:30:07.0	0.61	0.54	0.59685	0.54178	22.0	21.5	11.34
1403*	03:32:14.41	-29:17:05.8	03:32:13.86	-29:16:57.6	0.64	0.53	0.63664	0.63920	21.4	22.8	10.94
1600	10:01:30.53	+02:19:00.2	10:01:30.54	+02:18:57.5	0.96	0.49	0.98001	0.49714	22.3	-99.0	2.64
1601*	10:02:26.11	+02:46:10.9	10:02:26.25	+02:46:19.8	3.03	0.54	3.02746	0.53593	21.0	23.1	9.19
1602	10:02:03.38	+02:02:25.1	10:02:02.14	+02:02:24.4	0.43	0.36	0.42516	0.36434	21.1	21.1	18.54
1603	10:02:47.94	+02:29:28.2	10:02:47.17	+02:29:17.9	0.60	0.36	0.60936	0.36689	22.0	21.5	15.51
1604	10:01:30.50	+02:19:03.0	10:01:30.54	+02:18:57.5	0.69	0.49	0.69700	0.49714	22.8	-99.0	5.44
1605*	10:01:10.19	+02:32:42.4	10:01:10.49	+02:32:26.3	2.67	0.38	2.65219	0.37611	21.5	21.1	16.69
1606*	09:59:03.22	+02:20:02.9	09:59:03.83	+02:19:56.0	1.14	0.38	1.13109	0.37167	21.2	23.1	11.42
1607	09:59:43.12	+02:38:31.0	09:59:43.32	+02:38:20.7	0.55	0.51	0.54694	0.29322	21.7	23.2	10.69
1608	10:01:58.47	+02:03:50.6	10:01:57.79	+02:04:00.7	0.54	0.44	0.53148	0.43827	22.1	22.7	14.35
1609	10:01:50.91	+02:03:47.7	10:01:51.04	+02:04:04.2	0.54	0.35	0.53443	0.35523	21.8	22.2	16.65
1610*	10:00:28.63	+02:51:12.7	10:00:29.43	+02:51:07.2	0.78	0.73	0.76735	0.73089	21.5	23.1	13.28
1611	09:59:44.08	+02:33:01.7	09:59:44.48	+02:33:18.7	0.43	0.38	0.43934	0.37384	22.0	23.0	17.98
1612	10:00:14.81	+01:54:26.2	10:00:15.00	+01:54:06.6	0.68	0.36	0.67049	0.36038	21.9	23.0	19.78
1613	10:01:54.91	+02:04:19.4	10:01:55.73	+02:04:09.6	0.56	0.44	0.55452	0.43988	21.8	22.4	15.75

NOTE—Pair IDs marked with an asterisk indicate pairs with a broad-line AGN in the background object.

[a] Redshift determined from low-dispersion PRIMUS prism spectroscopy.

[b] Redshift determined from our Keck/LRIS or VLT/FORS2 followup spectroscopy. We failed to obtain spectra with S/N sufficient to constrain the redshift for targets with "—" these columns.

Table 2. Summary of Multislit Observations

Mask ID	R. A.	Declination	Pair Targets	Exposure Time (hrs)		Date
	J2000	J2000		Blue	Red	
			Keck/LRIS Spectroscopy			
XMM-1	02h 16m 10.135s	-04d 31m 02.341s	201, 202, 1207	2.06	1.90	2011 Oct 01
XMM-2	02h 21m 03.037s	-04d 53m 54.429s	210	2.17	2.04	2012 Jan 20
XMM-3	02h 20m 49.988s	-04d 33m 02.711s	208	1.67	1.57	2012 Jan 21
XMM-4	02h 20m 41.674s	-05d 32m 18.749s	213	0.9	0.78	2011 Oct 01
XMM-5	02h 17m 42.879s	-04d 13m 40.708s	204, 1209	1.40	1.33	2012 Jan 21
XMM-6	02h 15m 41.290s	-04d 27m 21.499s	203	3.17	2.93	2012 Dec 14-15
XMM-8	02h 19m 50.915s	-05d 12m 54.655s	221, 1202, 1204	0.92	0.37	2012 Dec 14
XMM-9	02h 17m 11.469s	-04d 38m 49.408s	223, 1203, 1205, 1206	1.33	1.25	2012 Dec 13
DEEP2 02^{h}-1	02h 32m 17.631s	+00d 46m 51.016s	302, 1300	1.00	0.89	2011 Oct 01
CDFS-1	03h 32m 05.670s	-29d 15m 39.128s	404, 405, 1403	1.80	1.67	2012 Dec 15
CDFS-2	03h 37m 01.165s	-28d 52m 08.792s	409, 1401	1.50	1.40	2012 Dec 15
COSMOS-1	10h 00m 35.040s	+02d 49m 32.190s	609, 610, 1610	2.08	1.96	2012 Jan 20
COSMOS-2	10h 00m 17.445s	+01d 54m 29.869s	620, 1612	1.33	1.26	2012 Jan 20
COSMOS-3	09h 59m 49.540s	+02d 29m 46.049s	606, 607, 1611	1.00	0.94	2012 Jan 20
COSMOS-4	09h 59m 40.738s	+02d 19m 37.569s	604, 621	1.67	1.56	2012 Jan 20
COSMOS-5	10h 01m 39.562s	+02d 16m 57.736s	603, 615, 1600, 1604	1.86	1.75	2012 Dec 14
COSMOS-6	10h 01m 09.715s	+02d 29m 16.189s	601, 1605	1.67	1.58	2012 Jan 21
COSMOS-7	10h 00m 11.443s	+02d 41m 08.694s	608	1.43	1.33	2012 Jan 21
COSMOS-8	10h 02m 45.330s	+02d 17m 34.108s	614	0.87	0.79	2012 Jan 21
COSMOS-9	09h 59m 32.490s	+02d 38m 19.718s	622, 1607	0.83	0.83	2012 Jan 21
COSMOS-10	10h 01m 49.901s	+02d 02m 52.574s	623, 1608, 1613	0.58	0.51	2012 Jan 21
COSMOS-11	10h 02m 50.485s	+02d 31m 39.362s	611, 1603	2.00	1.87	2012 Dec 15
COSMOS-12	10h 01m 34.027s	+02d 14m 45.950s	615, 624	1.50	1.34	2012 Dec 15
COSMOS-13	09h 58m 53.701s	+02d 26m 51.576s	617	1.19	1.14	2012 Dec 13
COSMOS-14	10h 01m 48.506s	+02d 03m 08.747s	626, 1602, 1609, 1613	2.50	2.22	2012 Dec 14-15
DEEP2 23^{h}-1	23h 31m 0.445s	+00d 06m 45.338s	103, 1100, 1101	0.78	0.75	2011 Oct 01
			VLT/FORS2 Spectroscopy			
XMM-7	02h 22m 19.336s	-05d 04m 25.90s	209, 211	3.00	0.50	2012 Nov 14-15
CDFS-1	03h 36m 39.326s	-28d 41m 49.360s	410, 411	1.38	0.25	2011 Nov 25
CDFS-3	03h 31m 12.198s	-28d 35m 39.69s	402, 403	0.83	0.50	2011 Nov 25
CDFS-4	03h 35m 13.89s	-28d 54m 57.14s	408, 1400	1.10	0.33	2011 Nov 25
CDFS-5	03h 35m 26.15s	-28d 46m 43.13s	412	0.92	0.25	2011 Nov 25
CDFS-6	03h 28m 10.935s	-28d 32m 39.720s	417	1.30	0.25	2012 Nov 15
CDFS-8	03h 35m 44.255s	-28d 21m 06.330s	413	0.99	0.25	2012 Nov 15
CDFS-9	03h 27m 55.600s	-29d 08m 10.750s	419	1.30	0.25	2012 Nov 15
CDFS-10	03h 36m 22.847s	-28d 28m 35.940s	414, 1402	1.50	0.25	2012 Nov 15
COSMOS-15	10h 01m 23.346s	+02d 30m 52.610s	602, 612	0.67	0.25	2011 Nov 25

NOTE—LRIS mask coordinates are given at the epoch of observation. FORS2 mask coordinates are given in the J2000 reference frame.

Table 3. Summary of Longslit Observations

Pair ID	Field	Exposure Time (hrs)		Date and Instrument[a]
		Blue	Red	
102	DEEP2 23^h	1.33	1.27	2012 Dec 15
104	DEEP2 23^h	0.50	0.48	2012 Dec 13
207	XMM	0.67	0.26	2012 Nov 14 (FORS2)
212	XMM	0.89	0.50	2012 Nov 14 (FORS2)
216	XMM	0.50	0.48	2012 Jan 20
217	XMM	0.61	0.53	2011 Oct 01
219	XMM	1.17	1.26	2012 Dec 13
301	DEEP2 02^h	0.50	0.48	2012 Jan 20
605	COSMOS	0.50	0.48	2012 Dec 13
613	COSMOS	0.50	0.48	2012 Dec 13
619	COSMOS	0.67	0.62	2012 Jan 21
625	COSMOS	0.44	0.33	2012 Nov 14 (FORS2)
1200	XMM	0.5	0.48	2012 Dec 13
1201	XMM	1.25	1.19	2012 Dec 13-14
1208	XMM	0.5	0.48	2012 Dec 13
1210	XMM	1.83	1.74	2012 Dec 13-14
1601	COSMOS	0.5	0.48	2012 Dec 13
1606	COSMOS	0.75	0.72	2012 Dec 13

[a] The instrument used is Keck/LRIS where not explicitly indicated.

Table 4. Foreground Galaxy Properties and CGM Absorption Line Measurements

Pair ID	$z_{f/g}$	M_B[a]	U-B[a]	$\log M_*/M_\odot$	SFR	$R_\perp$	S/N(Mg II)	W_{2796}	W_{2803}	$\langle\delta v_{2796}\rangle$
		(mag)	(mag)		($M_\odot$ yr^{-1})	(kpc)	(Å^{-1})	(Å)	(Å)	(km s^{-1})
101	0.4927	-20.99	0.68	10.02	8.2	45.6	18.7	1.116 ± 0.138	0.354 ± 0.105	-23.9
102	1.2440	—	—	10.68	18.1	26.6	6.0	2.183 ± 0.326	2.149 ± 0.364	-58.4
103*	0.4799	-20.34	0.80	10.11	2.7	30.5	3.2	0.100 ± 0.904	0.117 ± 0.830	-1.6
104*	0.4099	-19.23	0.70	9.54	1.2	34.6	35.8	-0.093 ± 0.074	0.165 ± 0.076	-73.4
201	0.4470	-20.14	0.82	9.77	0.9	43.1	6.2	-1.485 ± 0.400	-0.474 ± 0.398	-92.3
203	0.3514	-21.35	1.22	11.12	0.4	29.3	7.4	0.174 ± 0.339	-0.225 ± 0.355	67.1
204	0.4426	-21.52	1.22	11.08	0.9	21.3	11.4	0.012 ± 0.270	0.869 ± 0.249	-181.6
207*	0.4309	-20.47	1.09	10.60	1.2	42.0	20.1	-0.147 ± 0.110	-0.075 ± 0.129	-33.6
208*	0.5973	-21.83	0.99	11.07	8.4	17.2	13.6	2.012 ± 0.225	1.931 ± 0.261	183.8
209	0.3501	-19.38	0.55	9.37	1.7	11.0	9.2	1.297 ± 0.244	1.422 ± 0.216^b	-106.4
210	0.8062	-20.79	0.52	9.88	9.6	10.6	10.7	2.275 ± 0.247	1.902 ± 0.225	-28.4
211	0.4088	-21.22	0.84	10.68	3.1	25.5	10.4	1.878 ± 0.204	0.888 ± 0.210	-120.6
212*	0.5505	-19.94	0.70	9.79	2.0	44.7	12.6	0.084 ± 0.184	0.185 ± 0.192	22.6
213	0.4691	-20.21	0.55	9.40	3.4	15.1	11.1	2.558 ± 0.260	2.003 ± 0.252	28.1
217	0.3542	-20.87	0.70	10.26	6.5	34.1	5.6	0.608 ± 0.482	0.050 ± 0.478	-13.4
219	0.3688	-20.00	0.70	9.69	2.2	28.7	11.7	0.638 ± 0.233	0.214 ± 0.218	86.5
223*	0.7456	-20.59	0.73	9.66	4.2	44.0	4.5	0.203 ± 0.538	1.183 ± 0.612	0.7

Table 4 continued

Table 4 *(continued)*

Pair ID	$z_{f/g}$	M_B[a] (mag)	U-B[a] (mag)	$\log M_*/M_\odot$	SFR ($M_\odot$ yr^{-1})	$R_\perp$ (kpc)	S/N(Mg II) (Å^{-1})	W_{2796} (Å)	W_{2803} (Å)	$\langle\delta v_{2796}\rangle$ (km s^{-1})
301*	0.3628	-20.83	0.91	10.56	2.0	41.6	13.4	1.856 ± 0.221	2.128 ± 0.221	187.9
302	0.3505	-19.98	0.93	10.44	2.1	19.4	7.5	0.503 ± 0.380	0.752 ± 0.368	140.1
402*	0.5682	-19.91	0.54	9.44	2.7	35.4	5.2	1.179 ± 0.401^b	0.371 ± 0.393	-35.6
403*	0.5702	-20.14	0.72	9.80	2.0	44.7	5.0	0.268 ± 0.449	-0.304 ± 0.459	-138.0
404*	0.4328	-19.14	0.64	10.02	2.0	33.4	38.1	-0.066 ± 0.069	0.064 ± 0.069	139.4
405	0.3822	-20.31	1.23	10.65	0.2	39.1	7.9	0.729 ± 0.345	0.031 ± 0.305	-95.2
408	0.5974	-20.89	0.91	10.55	0.1	16.6	2.0	-1.768 ± 1.017	-1.008 ± 1.071	-43.0
409	0.3570	-20.38	0.62	10.18	2.1	46.1	3.0	1.536 ± 0.924	2.571 ± 0.871	43.9
410	0.5146	-20.04	0.46	9.16	3.5	41.6	3.5	0.184 ± 0.707	-0.459 ± 0.738	63.9
411	0.3668	-20.11	0.65	9.89	1.8	38.3	14.2	0.321 ± 0.161	-0.375 ± 0.192	97.5
412	0.7309	-20.99	0.53	10.11	6.1	26.5	7.1	0.363 ± 0.291	0.044 ± 0.321	-87.7
413	0.4275	-20.85	1.17	10.74	0.0	41.3	9.6	0.065 ± 0.204	0.727 ± 0.228	-3.1
414	0.4382	-19.95	0.57	9.69	5.7	40.8	11.2	0.073 ± 0.188	0.384 ± 0.168	-93.2
417	0.5688	-20.56	0.87	10.21	2.9	28.0	7.2	0.333 ± 0.294	-0.199 ± 0.290	-12.3
601	0.4929	-19.28	0.51	9.15	1.3	44.3	18.4	0.032 ± 0.141	-0.189 ± 0.136	-114.8
602*	0.5168	-20.16	0.66	9.87	2.5	40.5	21.6	0.225 ± 0.104	0.279 ± 0.111	50.5
603	0.6970	-22.55	1.11	11.24	1.2	20.1	19.1	-0.320 ± 0.136	0.339 ± 0.142	-194.7
604	0.2503	-20.58	0.52	9.07	0.7	13.2	2.0	-0.296 ± 1.270	-0.950 ± 1.243	-145.3
606	0.3466	-19.25	0.75	9.83	1.4	39.9	8.6	0.536 ± 0.356	0.625 ± 0.340	-78.1
608	0.5036	-21.16	0.78	10.52	5.5	14.6	15.3	1.567 ± 0.179	1.869 ± 0.186	133.7
609*	0.4376	-19.77	0.45	9.28	7.7	25.3	76.9	0.471 ± 0.034	0.419 ± 0.036	70.0
611	0.3516	-20.86	1.26	10.85	0.2	13.2	7.3	0.730 ± 0.317	1.091 ± 0.324	67.9
612*	0.3608	-19.09	0.16	9.00	5.5	12.2	29.0	1.235 ± 0.080	0.968 ± 0.087	-31.2
613*	0.7406	-21.06	0.61	10.11	11.0	26.2	17.2	2.286 ± 0.142	2.135 ± 0.146	89.7
614	0.3636	-21.94	1.26	11.41	0.3	22.8	3.3	1.816 ± 0.985^b	-0.378 ± 0.740^b	-153.7
617*	0.4881	-21.27	0.97	10.65	2.6	37.9	15.4	1.300 ± 0.189	1.043 ± 0.170	166.3
619	0.3524	-18.88	0.78	9.62	0.6	29.9	7.1	0.197 ± 0.355	-0.188 ± 0.316	102.1
621	0.3574	-20.29	0.53	9.74	5.5	47.2	6.4	0.718 ± 0.394	1.335 ± 0.419	104.2
623*	0.8258	-20.51	0.57	9.76	4.4	43.3	16.3	0.157 ± 0.146	0.017 ± 0.156	-63.9
624	0.3605	-20.46	0.82	10.29	2.7	21.5	7.6	1.504 ± 0.403	1.493 ± 0.369	-161.8
625*	0.6035	-19.77	0.55	9.44	1.9	37.1	14.5	-0.046 ± 0.139	-0.079 ± 0.155	29.0
626	0.4249	-20.64	1.07	10.65	0.6	31.0	4.5	1.008 ± 0.508	1.612 ± 0.550^b	49.6
1101	0.4072	-20.44	0.77	10.19	3.5	136.7	1.2	0.851 ± 2.324	0.866 ± 2.600	137.6
1201*	0.5653	-19.78	0.56	9.35	2.7	60.0	5.9	0.558 ± 0.402	0.538 ± 0.415	11.8
1202	0.4082	-20.30	1.33	10.89	0.1	128.8	9.0	0.040 ± 0.273	-0.085 ± 0.314	1.8
1205	0.3724	-20.92	1.26	11.03	0.1	65.2	11.9	-0.340 ± 0.239	-0.027 ± 0.203	-234.8
1207	0.7423	-21.19	0.96	10.69	3.4	131.0	25.2	2.038 ± 0.096	1.953 ± 0.100	29.1
1208*	0.8357	-21.75	0.55	10.41	19.2	56.5	16.1	1.119 ± 0.145	1.162 ± 0.136	-23.3
1209	0.3710	-21.01	0.96	10.68	2.3	94.1	14.3	0.247 ± 0.179	0.404 ± 0.175	76.1
1210*	0.5957	-21.16	0.99	10.68	3.5	55.5	7.6	1.264 ± 0.331	0.761 ± 0.320	-13.6
1300	0.5851	-19.92	0.77	9.71	1.8	101.9	22.7	0.269 ± 0.110	-0.073 ± 0.116	-84.4
1402	0.5418	-21.71	0.73	10.56	12.2	72.2	11.3	-0.383 ± 0.220	0.145 ± 0.200	-70.7
1600	0.4971	-20.52	0.69	10.06	5.3	16.1	19.8	2.005 ± 0.154	1.742 ± 0.151	154.7
1601*	0.5359	-20.05	0.62	9.72	2.9	58.1	28.4	2.529 ± 0.095^b	1.066 ± 0.100^b	8.9
1602	0.3643	-21.81	1.22	11.23	0.2	94.0	12.9	0.316 ± 0.208	0.212 ± 0.198	87.7
1603	0.3669	-20.72	0.88	10.51	4.4	79.0	15.6	1.617 ± 0.183^b	2.432 ± 0.211^b	-51.6
1604	0.4971	-20.52	0.69	10.06	5.3	33.1	10.6	1.519 ± 0.257	1.610 ± 0.267	130.0
1605*	0.3761	-21.51	0.94	10.89	13.9	86.3	36.7	0.769 ± 0.073^b	1.128 ± 0.072^b	-604.8

Table 4 continued

Table 4 *(continued)*

Pair ID	$z_{f/g}$	M_B[a] (mag)	U-B[a] (mag)	$\log M_*/M_\odot$	SFR ($M_\odot$ yr^{-1})	$R_\perp$ (kpc)	S/N(Mg II) (Å^{-1})	W_{2796} (Å)	W_{2803} (Å)	$\langle\delta v_{2796}\rangle$ (km s^{-1})
1606*	0.3717	-18.83	0.59	9.15	0.8	58.6	4.5	0.673 ± 0.577	0.636 ± 0.527	-75.2
1608	0.4383	-19.86	0.65	9.57	1.7	81.4	2.3	-1.315 ± 1.072	1.714 ± 1.052	257.8
1609	0.3552	-19.74	0.71	9.46	0.7	83.0	0.6	-1.537 ± 4.421	1.108 ± 4.582	-122.6
1610*	0.7309	-20.48	0.43	9.53	5.2	96.5	41.4	-0.031 ± 0.058	0.048 ± 0.059	50.3
1611	0.3738	-18.89	0.52	9.49	1.4	92.6	3.1	2.069 ± 0.760	-1.311 ± 0.865	-0.7
1612	0.3604	-19.10	0.76	9.40	0.7	99.6	11.7	-0.266 ± 0.229	-0.749 ± 0.233	-60.6
1613	0.4399	-21.20	1.20	10.74	0.2	89.5	4.5	1.982 ± 0.743[b]	1.121 ± 0.648	-71.5

NOTE—Pair IDs marked with an asterisk indicate pairs with a broad-line AGN in the background.

[a] Rest-frame photometric measurements are not available from Moustakas et al. (2013) for objects with blank entries in this column.

[b] Marks transitions affected by blending with Fe II absorption associated with the background galaxy, or with the Lyα forest.

Table 5. W_{2796} Dependence on Intrinsic Galaxy Properties

		All	$\log M_*/M_\odot$		SFR ($M_\odot$ yr^{-1})		$\log$ sSFR /yr^{-1}	
		PRIMUS Sample						
Subsample			< 9.9	> 9.9	< 2.5	> 2.5	< -9.46	> -9.46
$R_\perp < 30$ kpc	N	19	8	11	6	13	8	11
	Median W_{2796} (Å)	1.30	0.90	1.54	0.70	1.73	0.50	1.30
	Probability		0.892		0.049		0.222	
30 kpc $< R_\perp <$ 50 kpc	N	25	15	10	13	12	14	11
	Median W_{2796} (Å)	0.27	0.20	1.06	0.12	0.62	0.25	0.36
	Probability	0.003	0.006		0.306		0.973	
		QSO-Galaxy Comparison Sample						
Subsample			< 10.1	> 10.1	< 1.3	> 1.3	< -10.0	> -10.0
$R_\perp < 30$ kpc	N	19	13	6	13	6	6	13
	Median W_{2796} (Å)	0.80	0.87	0.75	0.76	0.80	0.71	0.87
	Probability		0.726		0.661		0.792	
30 kpc $< R_\perp <$ 50 kpc	N	31	6	25	12	19	15	16
	Median W_{2796} (Å)	0.43	0.20	0.55	0.31	0.71	0.39	0.48
	Probability	0.024	0.017		0.003		0.736	

NOTE—Two-sample comparisons use Gehan's generalized Wilcoxon test of the probability that the two W_{2796} distributions in question are drawn from the same parent population.

APPENDIX

A. KECK/LRIS AND VLT/FORS2 BACKGROUND GALAXY SPECTROSCOPY

Figure 18 shows our spectroscopy of all PRIMUS background sightlines in the region surrounding Mg II in the rest frame of the foreground galaxy. The ID number of each pair is indicated in the upper left corner of each panel.

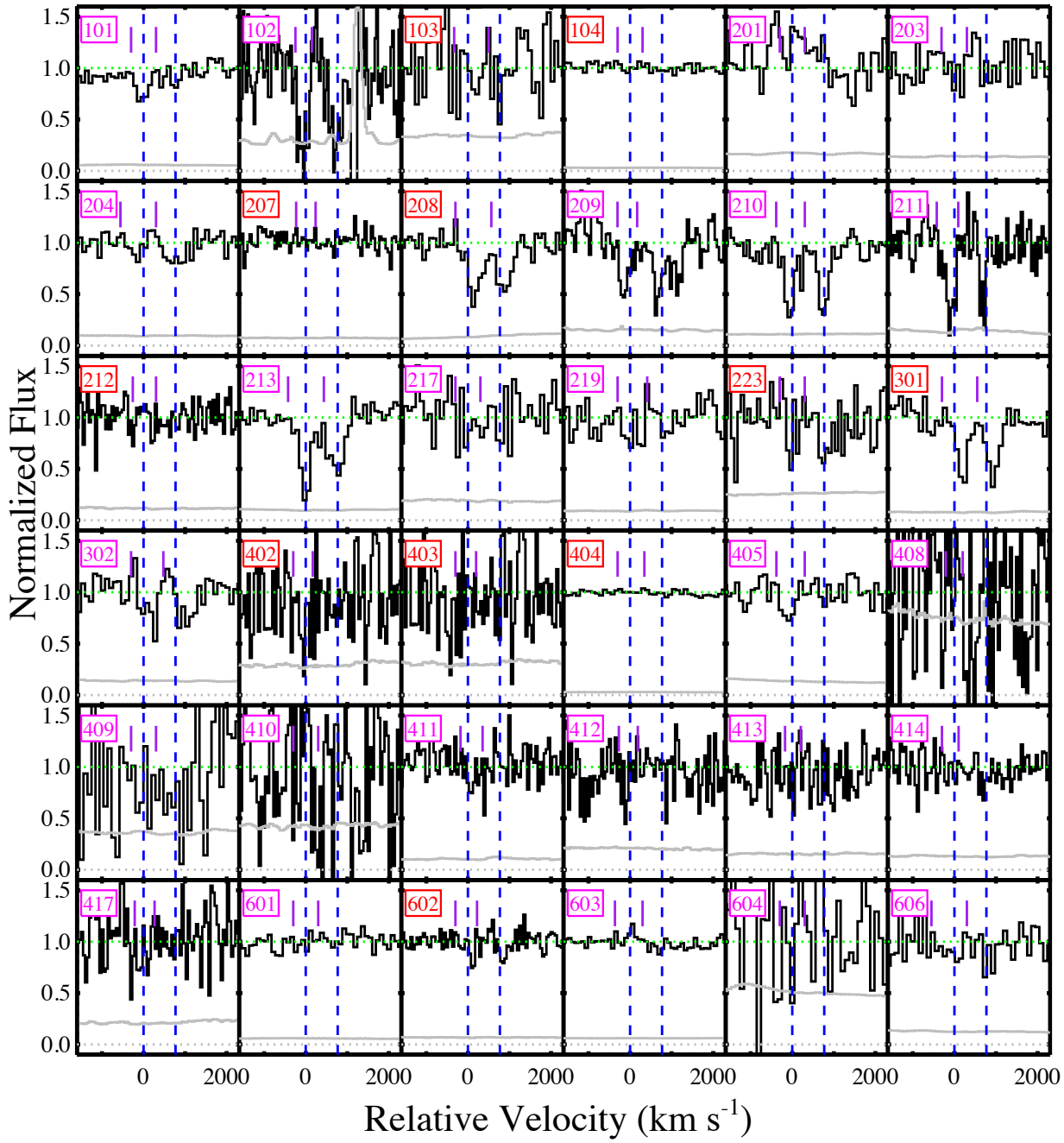

Figure 18. Background galaxy spectroscopy covering the Mg II $\lambda\lambda 2796, 2803$ doublet at the systemic velocity of the paired foreground galaxy. The pair ID is printed in red for those pairs with b/g galaxies hosting broad-line AGN, and is printed in magenta for the remaining pairs. The relative velocity is 0 km s^{-1} at the wavelength of the Mg II 2796 transition at $z_{\rm f/g}$, with the blue vertical dashed lines indicating the velocities of both doublet transitions. The gray histogram shows the error in each spectral pixel, and the green dotted curve marks the continuum level. The two vertical purple hashes indicate the velocity range adopted in our calculation of the boxcar W_{2796}.

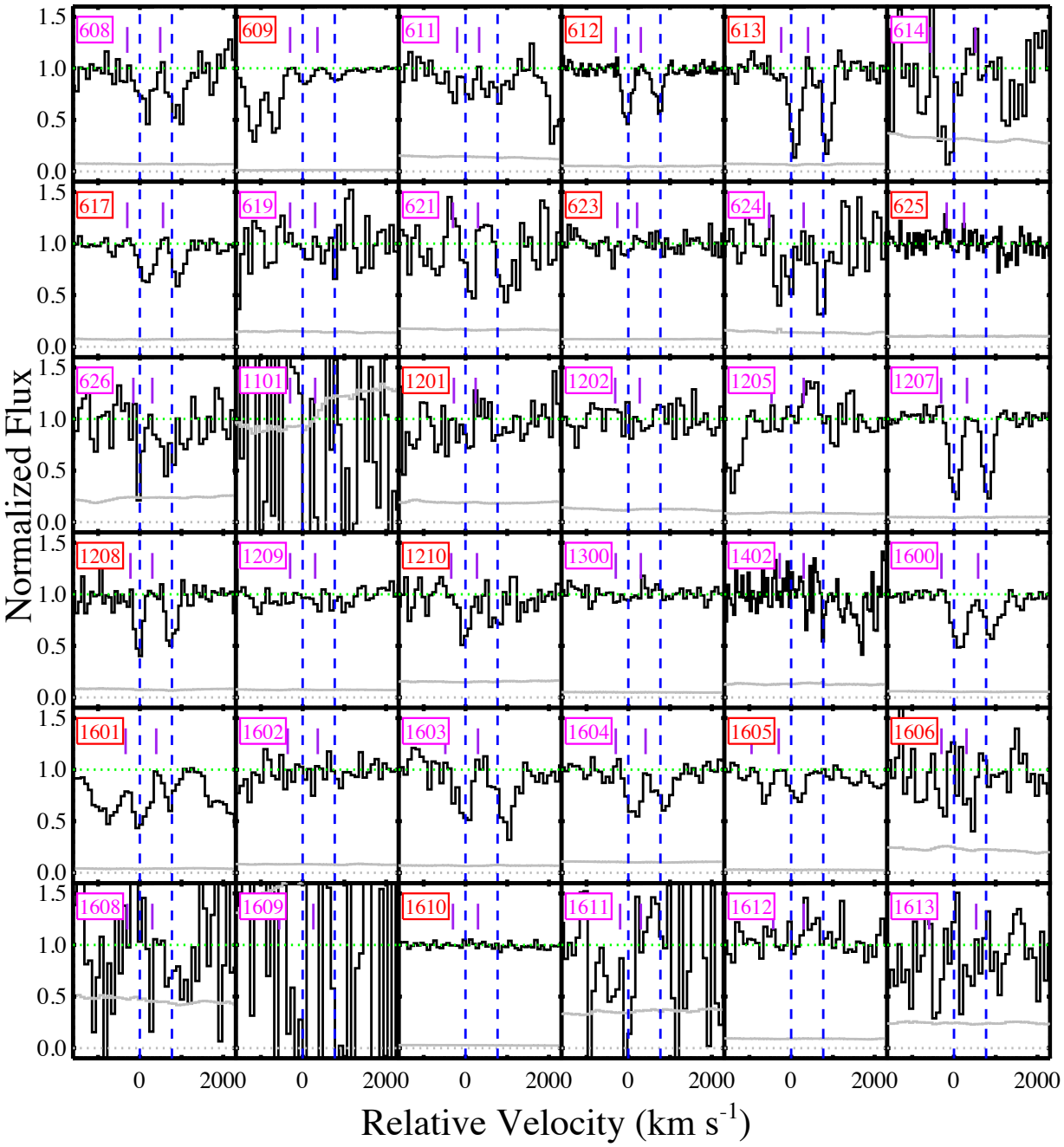

Figure 18. – continued